Available online at www.sciencedirect.com

ScienceDirect

Advances in Space Research xxx (xxxx) xxx

ADVANCES IN SPACE RESEARCH (a COSPAR publication)

www.elsevier.com/locate/asr

High-speed echoes in the polar winter mesosphere: Infrasound as a probable cause

Evgenia Belova [a], Victoria Barabash [b,*], Oleg A. Godin [c], Johan Kero [a], Sven Peter Näsholm [d,e], Ekaterina Vorobeva [d,f], Alexis Le Pichon [g]

[a] Swedish Institute of Space Physics, Box 812, S-981 28 Kiruna, Sweden
[b] Luleå University of Technology, Box 848, S-981 28 Kiruna, Sweden
[c] Naval Postgraduate School, Monterey, CA 93943, USA
[d] NORSAR, P.O. Box 53, N-2027 Kjeller, Norway
[e] Department of Informatics, University of Oslo, P.O box 1080 Blindern, N-0316 Oslo, Norway
[f] Norwegian University of Science and Technology, Postbox 8900, NO-7491 Trondheim, Torgarden, Trondheim, Norway
[g] CEA, DAM, DIF, F-91297 Arpajon, France

Received 7 February 2023; received in revised form 2 June 2023; accepted 5 July 2023

Abstract

We considered three events on 4 November 2015, 22 December 2016, and 12 November 2018, when the signals travelling in the polar winter mesosphere with high horizontal velocities above 300 m/s were measured by the atmospheric radar ESRAD (Chilson et al., 1999) located at Esrange, near Kiruna in northern Sweden. We proposed four mechanisms of generation of such special cases of polar mesosphere echoes, e.g. high-speed PMWE, that involve microbaroms, i.e. infrasound waves at 0.1—0.35 Hz frequencies created by ocean swell. These mechanisms are (i) generation of viscous waves, (ii) generation of thermal waves, (iii) direct contributions of infrasound, and (iv) generation of secondary waves at sound dissipation. These processes necessarily accompany sound propagation in inhomogeneous, thermally conducting and viscous fluid (air). The four models were theoretically analysed and their efficiency was estimated. The infrasound measurements at the IS37 station (Gibbons et al., 2019) located about 170 km north-west from the ESRAD radar, modelled maps of the microbarom sources, infrasound propagation conditions and ionospheric conditions for these three PMWE events support the proposed models. Infrasound-generated thermal waves are suggested to be the most probable specific cause of the observed high-speed, high-aspect-ratio PMWE events. However, absence of in-situ infrasound and plasma measurements did not allow us to quantify contributions of individual physical mechanisms to the fast-travelling echoes generation.

Keywords: Polar mesosphere winter echoes; Infrasound waves; Microbaroms; Energetic particle precipitation; Solar wind; High-speed PMWE

1. Introduction

Polar mesosphere echoes are strong signals from 50 to 100 km altitudes observed by radars operating at a broad frequency range, i.e. from a few to hundreds of MHz, at polar latitudes all over the year. The echoes observed from May to August in the northern hemisphere were named polar mesosphere summer echoes (PMSE) (Röttger et al., 1988). In contrast, echoes that occur in the equinox and winter seasons were later named polar mesosphere winter echoes (PMWE) (Kirkwood et al., 2002). Therefore, when we mention 'winter' further in this paper, this refers to all non-summer months. Mesospheric echoes have been intensively studied for several decades (for reviews and references see Rapp and Lübken, 2004; Strelnikov et al.,

* Corresponding author.
E-mail address: victoria.barabash@ltu.se (V. Barabash).

https://doi.org/10.1016/j.asr.2023.07.010
0273-1177/

2021). Differences between the summer and winter mesospheric radar returns were first reported by Ecklund and Balsley (1981). Later these findings were quantified by subsequent observations over a full year. E.g., based on two-year continuous observations with the Moveable Atmospheric Radar for Antarctica (MARA) at the Antarctic station Troll, Kirkwood et al. (2015a) showed that, in winter these echoes were significantly weaker than in summer, and that they come from lower altitudes, 55–80 km. Whereas in summer, the radar echoes arose from altitudes between 80 and 95 km and were more frequent and intense. Similar results were obtained with the Middle Atmosphere Alomar Radar System (MAARSY) (Latteck et al., 2012) at Andøya, northern Norway by Latteck and Strelnikova (2015). The PMWE mean diurnal occurrence rate estimated from MAARSY data for the winter seasons of 2011–2013, was 16% (95% for PMSE in June/July). Latteck et al. (2021) conducted a comprehensive study of the mesospheric echo characteristics at Andøya based on ALomar WINd (ALWIN) radar data for 1999–2008 and the following MAARSY radar data for 2011–2020. It was found that the 17 dB more sensitive MAARSY system observed echoes below 80 km all year round with a mean seasonal occurrence frequency of about 14% with strong variations from minimum of 2% in July/August and maxima of 22% and 26% in March/April and October, respectively. When only non-summer months were considered, the average PMWE occurrence rate was estimated to be 17.5%, thus confirming the results of the earlier study. Latteck et al. (2021) also found that PMSE can be up to 3 orders of magnitude stronger than PMWE.

PMWE are often observed when the electron number density in the mesosphere is strongly enhanced (e.g., Kirkwood et al., 2002; Nishiyama et al., 2018). Extra ionisation in this region can be produced by solar protons and X-rays related to coronal mass ejections and solar flares, respectively. Additionally, high-speed solar wind streams (HSS) emanated from the coronal holes, upon arrival at the Earth cause high-energy electron precipitation from the magnetosphere (e.g., Meredith et al., 2011) that leads to significant ionisation at PMWE altitudes (Kavanagh et al., 2012; Kirkwood et al., 2015b). The PMWE occurrence rate of 60% of all winter days observed with MARA was mainly attributed to the arrival of HSS (Kirkwood et al., 2015a). Latteck and Strelnikova (2015) reported that the diurnal occurrence rate reached 70% during solar proton events or strong geomagnetic disturbances.

In order to detect PMSE/PMWE by radars, electron density fluctuations have to exist on the radar Bragg scale, which varies from tens of cm to a few metres for monostatic very high frequency (VHF) radars. It was found that PMSE are directly related to very low temperatures at the polar summer mesopause (e.g., Lübken, 1999), where ice particles of nano-metre size are formed (e.g., Baumgarten et al., 2008; Hervig et al., 2009). It is now commonly accepted (e.g., Rapp & Lübken, 2004) that neutral air turbulence in presence of charged ice aerosols leads to generation of small-scale perturbations in the electron number density at the mesospheric altitudes that results in the strong radar returns, i.e. PMSE. However, in winter the mesospheric temperatures are much higher than in summer, and therefore, ice particles cannot form. Instead, other smaller particles of meteoric origin, i.e. meteor smoke particles (MSPs), have been observed in the winter mesosphere (e.g., Rapp et al., 2009; Baumann et al., 2013, Robertson et al., 2014). It was shown that charged MSPs play an important role in PMWE appearance and features (Kirkwood et al., 2015a).

Numerous efforts have been made in order to understand the PMWE nature and its observed characteristics. Recently, Strelnikov et al. (2021) provided a short overview of PMWE current theories, which can be generally divided into two categories related to turbulent and non-turbulent origin. It was found that a majority of PMWE can be explained by the neutral air turbulence with or without the presence of MSPs (e.g. Staszak et al., 2021). However, in some cases strong, quasi-specular radar echoes with high horizontal speeds exceeding 350–400 m/s were observed (Kirkwood et al., 2006; Kirkwood, 2007). Since atmospheric scatterers moving with velocities of hundreds of m/s cannot be attributed to the atmospheric turbulence or nano particles moving with the wind, there is a need to understand what are the physical mechanisms that can generate polar mesospheric echoes with a very high horizontal travel velocity, e.g. high-speed PMWEs.

This paper investigates the hypothesis that fast-travelling PMWEs result from the electron density perturbations created in continuously stratified atmosphere by low-frequency acoustic waves (infrasound), specifically, by microbaroms. Microbaroms dominate the ambient acoustic field from the stratosphere to the mesosphere, and typically have frequencies between 0.1 and 0.35 Hz. Microbaroms are generated by nonlinear interaction of surface gravity waves in the ocean, most efficiently at several hotspots around the globe (e.g., Le Pichon et al., 2010 and the references therein). The Northern hemisphere hotspots include parts of the North Sea and the wider Northern Atlantic Ocean (e.g., Landès et al., 2014). Microbaroms can propagate through the atmosphere over thousands of km due to their low absorption (Sutherland and Bass, 2004) and channelling by stratospheric, and mesosphere-lower thermospheric (MLT) waveguides (Drob et al., 2003). Ocean swell and long-periodic wind-associated waves on the ocean surface are known to be intermittent and form wave groups (wave packets) (Longuet-Higgins, 1984), which translate into the atmospheric microbaroms travelling from their generation sites as narrow-band acoustic wave packets. Locally, an individual infrasonic sound wave packet can be viewed as a plane wave with a gradual amplitude modulation occurring at larger horizontal scales compared to the acoustic wavelength. The wave packets travel at the acoustic group speed, which is a vector sum of the wind velocity $\boldsymbol{u}$ and the sound speed c in the direction of propagation relative

to air. Depending on the wind direction and the direction of sound propagation, the horizontal component of the wave packet speed lies between $c - u$ and $c + u$ (e.g., Brekhovskikh & Godin, 1999).

Generation of high-speed PMWE involves a cascade of physical processes. In a real atmosphere, which is viscous, thermally conducting, and continuously stratified in the vertical direction, a propagating infrasonic wave packet creates perturbations in the neutral atmosphere at vertical spatial scales that are small compared to the acoustic wavelength. In the presence of ionisation, the neutral component perturbations cause commensurate changes in the free electron density and the radio wave refraction index. The spatial variation of the refraction index, specifically, its spectral component at the Bragg scale of the incident radio wave, leads to radio wave scattering (reflection) and occurrence of radar echoes (e.g., Gage & Balsley, 1980). Since the perturbations in the neutral atmosphere and in the electron number density are proportional to the infrasound amplitude, the atmospheric reflectors are predicted to move horizontally with the infrasonic wave packet at a speed between $c - u$ and $c + u$, or roughly within 100 m/s of the sound speed $c \sim 250$–400 m/s at the altitude of PWME generation. This explains the observed range of speeds of fast-travelling PMWE (Kirkwood et al., 2006). The vertical scale of the atmospheric inhomogeneities responsible for PMWE is at close to half the radio wavelength (less than a few meters for VHF radars) and the horizontal scale of the infrasound induced inhomogeneities is of the order of microbarom wavelength of ~ 1 km. Therefore, the atmospheric reflector is highly anisotropic, and the radar scattering closely approximates specular reflection from a horizontal interface. The anisotropy of this infrasound-generated reflector explains another distinctive observational feature of the fast-travelling PMWE: their high aspect sensitivity (Kirkwood et al., 2006).

The central part of the proposed explanation of the origin of the fast-travelling PMWE is the physical mechanism where infrasound generates vertical variations of the radio wave refraction index at the radar Bragg scale. We show in Sec. 3 and in the Appendix that the requisite variations in the refractive index can occur in a continuously stratified atmosphere due to excitation of the strongly evanescent viscous and thermal waves (Pierce, 1989; Brekhovskikh and Godin, 1998). Hocking et al. (1991) and Hocking (2003) were the first to propose that viscous and thermal waves, which are generated at reflection of gravity waves and infrasound and which are strongly evanescent in the vertical direction, cause highly aspect-sensitive radar echoes that cannot be attributed to turbulence. Properties of the viscous and thermal waves were considered assuming reflection of infrasound or gravity waves at a single sharp interface in the atmosphere. This model was used to interpret the near-specular reflections observed with a 50 MHz radar (Hocking et al., 1991). Kirkwood et al. (2006) successfully used Hocking's idea of strongly evanescent waves generated at the reflection of infrasound to interpret key observational features of fast-travelling PMWEs that occurred during a solar proton event in November 2004 which were observed by the 52-MHz ESrange RADar (ESRAD) and the 224-MHz European Incoherent SCATter (EISCAT) radars. It was found that the spectral width of the EISCAT radar echoes inside PMWE is the same as for the background plasma below and above PMWE. From their PMWE morphology analyses, horizontal travel speed, and spectral width, Kirkwood et al. (2006) concluded that fast-travelling PMWE can be most reasonably explained by physical mechanisms that involve infrasound.

The present work shares the central hypothesis of Hocking et al. (1991), Hocking (2003) and Kirkwood et al. (2006) regarding the role of strongly evanescent waves generated by infrasound. However, we replace the heuristic arguments of Hocking et al. (1991) and Hocking (2003) with a consistent theory for the viscous and thermal wave excitation and radio wave refraction index perturbation generated by infrasound. The Appendix contains a detailed theoretical analysis, while the results and implications are discussed in Sec. 3. In contrast to reflection from a sharp interface (Hocking et al., 1991; Hocking, 2003), the refraction index perturbations are strongly affected by interference of evanescent waves generated at different altitudes in a real, gradually varying atmosphere. The notion of resonance scattering of radio waves by evanescent waves, which was postulated by Hocking et al. (1991) and Hocking (2003) and implied in (Kirkwood et al., 2006), is not supported by the developed theory. We also show that generation of viscous and thermal waves and the occurrence of high-speed PMWE does not necessarily require reflection of infrasound or strong temperature or wind speed gradients. In Sec. 2, we describe and analyse three recent PMWE events with a high horizontal travel speed, observed by the atmospheric VHF radar ESRAD (Chilson et al., 1999) at Esrange, northern Sweden. Evidence is presented in Sec. 4 that the necessary conditions for fast-travelling PMWE occurrence, namely, presence of strong microbaroms and elevated electron number density at the altitudes of the PMWE generation, were met. For these three events we present the infrasound measurements at IS37 station (e.g., Gibbons et al., 2019) in Bardufoss, Norway located 170 km north-west of ESRAD together with information about microbarom sources and infrasound propagation conditions. Our findings are summarised in Sec. 5.

2. PMWE observations

2.1. Overview of the radar instrumentation and data

ESRAD is a mesosphere-stratosphere-troposphere (MST) radar located at Esrange (67.9° N, 21.1° E), near Kiruna, northern Sweden. It has been in continuous operation since 1996. This radar provides information on the dynamic state of the atmosphere - winds, waves, turbulence

and layering, from the troposphere up to the mesopause (ca. 1–95 km altitude). It operates at 52 MHz with a vertical beam, with a beamwidth of about 5°, and the signal is scattered back from irregularities in the refractive index of the air. The nominal peak transmit power is 72 kW, however, because of progressive failure of several power blocks during the last few years, the power has gradually been reduced to 18 kW at present. The ESRAD antenna array, consisting of 284 Yagis, is divided into 12 identical groups (6 groups before December 2015). The radar transmits vertically with the whole antenna array, but for reception one can use 12 segments in different combinations. More detailed descriptions of ESRAD can be found in Chilson et al. (1999) and Belova et al. (2021). The radar runs continuously, cycling between experimental modes optimised for the lower troposphere, troposphere/stratosphere, or mesosphere. A typical cycle measures for about 1 min in each mode, repeating every 3–4 min.

Vertical wind is derived from the Doppler shift of the return signal by coherently combining the data from all receivers. Horizontal winds are derived by using the full correlation analysis (FCA) method developed by Briggs et al. (1950) and Briggs (1984). The principle behind FCA is that an ensemble of scatterers of the radar wave in the atmosphere leads to a diffraction pattern on the ground that moves across the antenna array, as the scatterers move horizontally advected by wind. With transmission at the whole array, for reception we use three non-collinear antenna subarrays consisting of four groups of antennas each. Signals from these four groups are added coherently to improve the signal-to-noise ratio. The arrangement of the receivers was shown by Belova et al. (2021). Zonal and meridional velocity components are derived using auto- and cross-correlations between the different antenna subarrays to account for the scatterers' decay. For ESRAD we adopted the FCA algorithm as described by Holdsworth (1995).

We apply several quality checks for inferred velocities. These FCA quality control criteria include that normalised time delay between the subarrays is less than 0.4, spatial correlation shape is limited to the ellipse, mathematically successful fitting of the velocities, and a high-enough signal-to-noise ratio (SNR). The meteors were also disregarded. In this study we used a value of 0.9 as SNR rejection threshold. This was subjectively chosen based on a compromise between the number of observations that passed quality control and quality of the data set. When we apply a value of 1 for the threshold, we still have these high-speed values, e.g. above 300 m/s, meanwhile, the number of other data points is reduced.

We used the data from the operating modes covering the mesosphere and lower thermosphere (50–100 km): mode 'fca_4500′ was in operation until April 2016, then it was changed to 'fca_900′. The parameters of the experiments are shown in Table 1. The velocity profiles were calculated with about 1 min. resolution and the measurements in these modes were repeated every fourth minute.

2.2. Satellite and ground-based data

As mentioned before, the high PMWE occurrence rate might be related to extra ionisation in the middle atmosphere at the associated altitudes. This can be caused by solar protons, solar X-rays and high-energy electrons precipitating from the magnetosphere after the arrival of HSS at the Earth (e.g., Tanaka et al., 2019). For this study, we analysed satellite measurements of the solar proton and X-ray fluxes, and solar wind velocity provided by the Geostationary Operational Environmental Satellites (GOES) and the Deep Space Climate Observatory (DSCOVR) satellite. The respective datasets are available through the database of the Space Weather Prediction Center at National Oceanic and Atmospheric Administration/.

(https://www.swpc.noaa.gov/products/).

For local monitoring of ionisation in the lower ionosphere, two ground-based Relative Ionospheric Opacity meters (riometers) were used. A riometer is a radio receiver that continuously measures cosmic noise at the ground after the noise has passed through and has been absorbed within the ionosphere. By comparing the observed level and known quiet day level, one can measure additional cosmic noise absorption (CNA) due to elevated electron density caused by e.g., energetic electron precipitation associated with HSS. The CNA occurs primarily in the D-layer of the ionosphere at 60–90 km altitude. Measurements of radio noise absorption (as a proxy for energetic particle precipitation and ionisation at PMWE altitudes) in this study were provided by the La Jolla fast-response solid-state riometers observing at 30 and 38 MHz, which were operated in Kiruna [dataset] (https://www2.irf.se/Observatory/?link=Riometers) [dataset] Kiruna riometers https://www2.irf.se/Observatory/?link=Riometers.

2.3. PMWE events

Unlike PMSE occurring almost every day during summer months, the winter mesospheric echoes have been observed by ESRAD only sporadically. Among all PMWE observations the echoes with the high horizontal travel speed are very rare.

We have screened the data for days with PMWE moving with horizontal velocity above 350 m/s, for the period starting from December 2013, the time when the microbarom measurements at IS37 in Bardufoss, Norway were started, until December 2020. Seven days were found and from these, three longer lasting PMWE events were selected for the study. After 2018, ESRAD gradually lost 75% of its transmitter power, which implies that only very strong echoes could match the FCA quality criteria to allow horizontal velocities to be estimated.

2.3.1. Event 1: 4 November 2015

The PMWE were observed by ESRAD on 4 November 2015 and echo SNR, aspect sensitivity, horizontal velocity

Table 1
Parameters of the ESRAD modes used in the paper.

Date	4/11/2015	22/12/2016 and 12/11/2018
Mode name	fca_4500	fca_900
Pulse repetition frequency	1300 Hz	1300 Hz
Code	8-bit complementary	none
N of coherent integrations	32	64
Time resolution	49.2 ms	49.2 ms
Height sampling/ resolution	600 m / 600 *m*	600 m / 900 *m*
Duration	60 s	80 s
How often	20 h^{-1}	17 h^{-1}

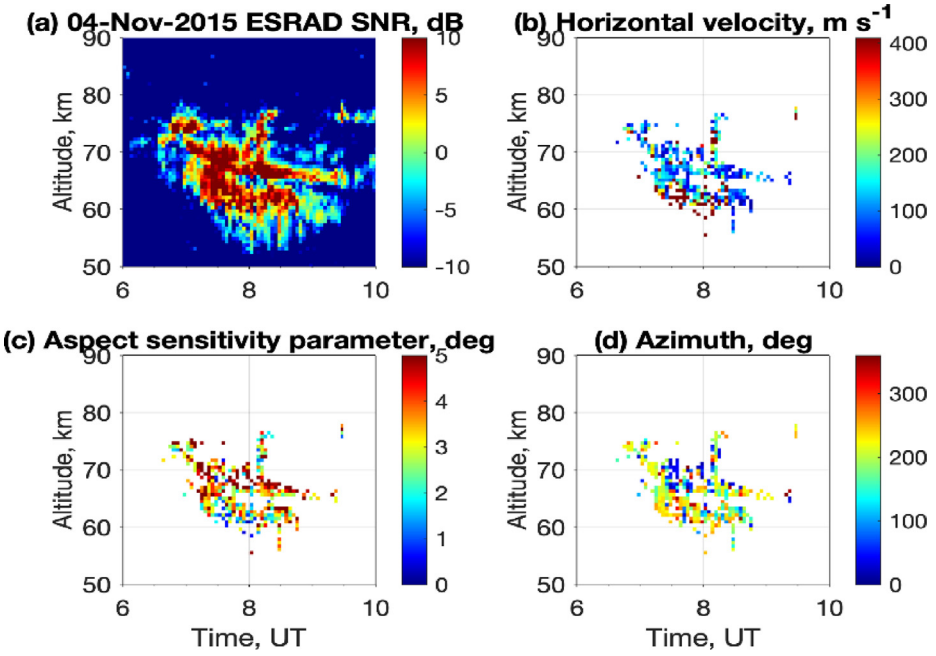

Fig. 1. PMWE on 4 November 2015 observed by the ESRAD radar: (a) signal-to-noise ratio (SNR), (b) horizontal velocity magnitude, (c) aspect sensitivity parameter, (d) azimuth angle of horizontal velocity, the azimuth angle shows where the echo is propagating.

magnitude and azimuth angle are presented in Fig. 1. The aspect sensitivity parameter of echoes is defined as a half-power half-width θ_s of the scatterers' polar diagram (e.g. Swarnalingam et al., 2011). It was calculated by using the parameters of the diffraction pattern, estimated by the FCA and the radar beam widths for transmission and reception. See Smirnova et al. (2012) for more details. The smaller aspect sensitivity parameter corresponds to higher aspect sensitive scatterers, i.e. aspect sensitivity parameter of 0° implies specular reflection. The layers of enhanced backscatter were observed between 52 and 78 km altitude for about 3 h, between 6:30 UT and 9:30 UT. The echoes were strong with a signal-to-noise ratio (SNR) above 10 dB. For this event, most of the horizontal velocities were less than 100 m/s. However, mainly at the lower edge of the strongest echoes, very high speeds above 350 m/s were also observed. These echoes are highly aspect sensitive with θ_s of about 0.5°-1.5°. The echo velocities have not been estimated for low SNR, since these signals did not fulfil the FCA quality criteria described in Section 2.1.

Meredith et al. (2011) showed that the high-energy electron precipitation starts when the solar wind speed increases sharply from below 400 km/s to above 450 km/s (this indicates the arrival of HSS at the Earth) and can last for several days. Solar wind speed (not shown) measured by the DSCOVR satellite increased, reaching more than 450 km/s already on November 3. Solar wind speeds above 600 km/s were observed during the entire day of November 4, indicating progressive electron precipitation. Additionally, the burst of the enhanced X-ray flux was observed on the same day around 12:00 UT, i.e. after the PMWE. The solar proton flux was on an undisturbed level. The Kiruna 30 MHz riometer showed increased cosmic noise absorption between 01:00–12:00 UT, with a maximum absorption of 6 dB at 8:00 UT. This indicates strong ionisation of the ionospheric D-layer.

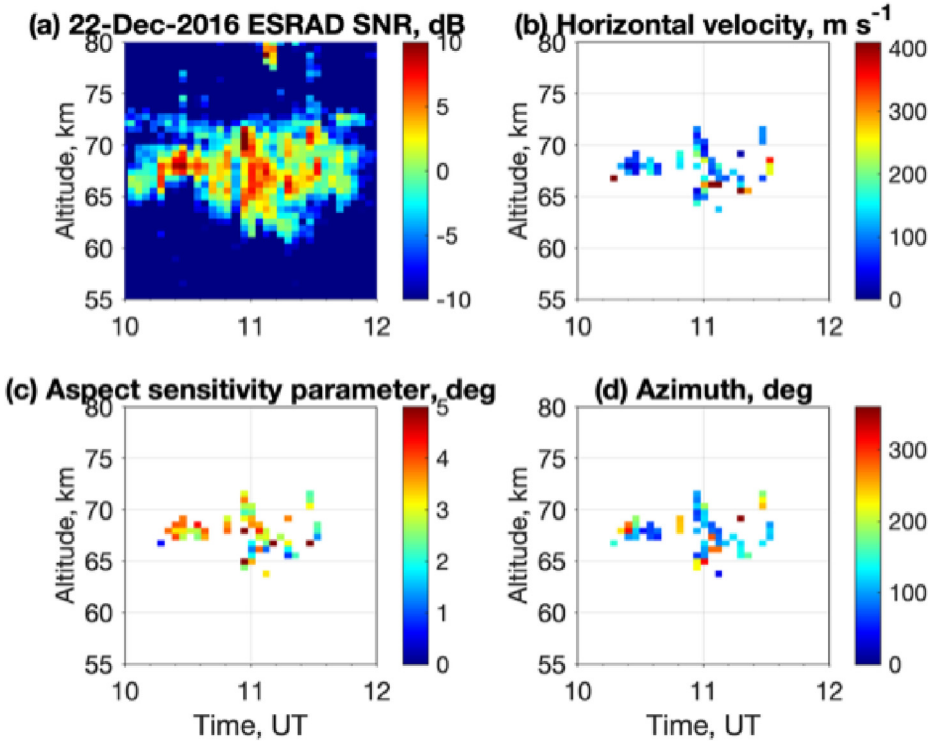

Fig. 2. The same as Fig, 1, but for the PMWE event on 22 December 2016.

2.3.2. Event 2: 22 December 2016

The PMWE on 22 December 2016 (Fig. 2) are weaker than the event on 4 November 2015. The layer of enhanced backscatter occurs between 60 and 73 km and lasts for about 2 h. There are also several patches of echoes above the main layer lasting for a few minutes. Because of the lower SNR, few reliable velocity estimates were retrieved using FCA. Only on a few occasions at 65–66 km the horizontal velocity exceeded 300 m/s and the echoes showed high aspect sensitivity.

The solar wind speed was enhanced above 600 km/s during the entire day, indicating progressive action of HSS on the Earth. There was neither indication of a solar proton event nor solar X-ray flare. Both the Kiruna riometers showed moderately elevated absorption (up to 2 dB) from 9:00 UT to 12:00 UT, the time when PMWE were observed (not displayed).

2.3.3. Event 3: 12 November 2018

On 12 November 2018, two separate PMWE layers (Fig. 3) were almost simultaneously observed by ESRAD. The lower layer, at about 65 km, varied significantly in strength and thickness between 8:00 UT and 10:00 UT. The upper layer, at about 75 km, had higher SNR and lasted for about one hour. Velocities exceeding 300 m/s were registered at 72 km altitude.

The solar wind speed varied between 540 and 650 km/s during the entire day. The solar proton and X-ray fluxes remained at background levels. The cosmic noise absorption measured by the Kiruna 30 MHz riometer increased up to 2 dB during the PMWE event.

3. Possible physical mechanisms of high-speed PMWE generation by infrasound

As pointed out in the Introduction, scatterers moving at speeds of hundreds of m/s cannot be attributed to atmospheric turbulence or microparticles moving with the wind. Furthermore, observations of radar reflections with high aspect sensitivity (see Sec. 2 and Kirkwood et al., 2006) show that scatterers retain phase coherence over hundreds of metres horizontally.

Acoustic wave of frequency f and horizontal component k of the wave vector, the phase of pressure, density perturbations and particle velocities move horizontally with the speed $2\pi f/k$, which is of the order of the sound speed, $c \sim$ 250–400 m/s, or larger. The absorption of acoustic waves increases with altitude z as $f^2/\rho_0(z)$ (Sutherland and Bass, 2004), where ρ_0 is the mass density of air. Therefore, only low-frequency sound (infrasound) is expected to be present at the MLT altitudes, with microbaroms as its dominant component (e.g., Le Pichon et al., 2010). The horizontal spatial scale of the acoustic wave phase variations, $2\pi/k \sim c/f$, is about 1–3 km for typical microbarom frequencies $f = 0.1$–0.35 Hz. Thus, infrasound has the requisite properties to explain the high-speed PMWE observations described in Sec. 2, if the infrasound-induced perturbations of the neutral atmosphere are translated into

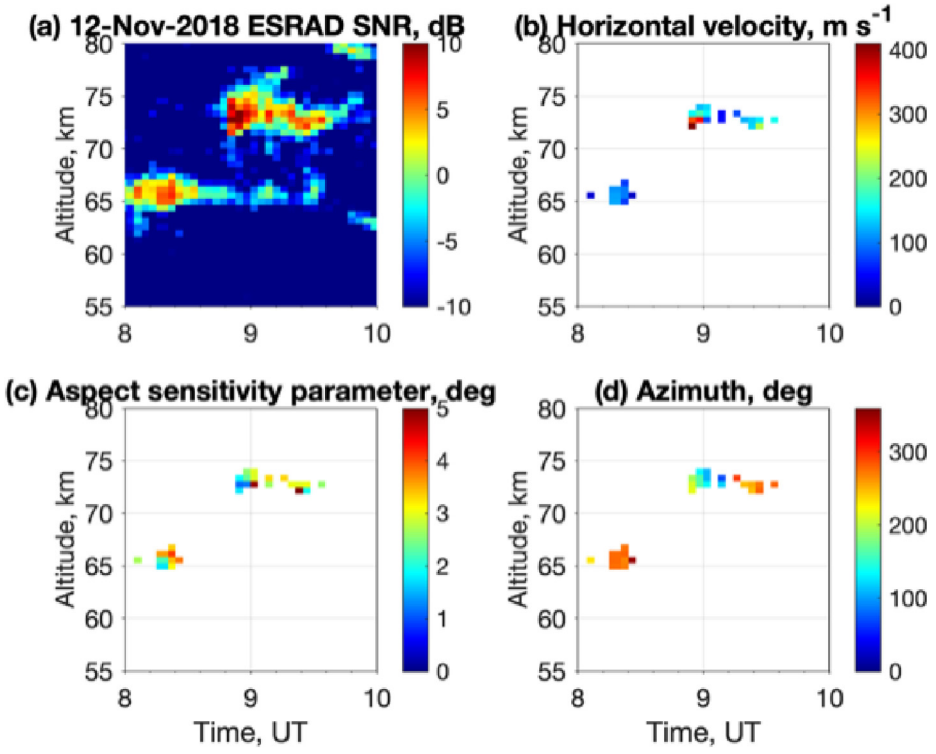

Fig. 3. The same as Fig, 1, but for the PMWE event on 12 November 2018.

the vertical gradients $\partial n/\partial z$ of the radio wave refraction index, which are responsible for radar wave reflections (e.g., Gage and Balsley, 1980).

Motion of the neutral component of the atmosphere entrains ions, which in turn affects electrons and the refraction index n of VHF radar waves. Modulation of the ambient electron density N_0 by mechanical waves results from perturbations in the air mass density and particle motion in the direction of the gradients (presumed vertical) of N_0 and ρ_0. The specular reflection amplitude of a radar pulse is mostly sensitive to the spectral component of $\partial n/\partial z$ at the radar Bragg scale (half-wavelength of the radio wave), but the reflection amplitude can also be significant when $|\partial n/\partial z|$ is sufficiently large in a layer that is thinner than the radar vertical resolution (see the Appendix). Vertical scales of mass density perturbations and particle motion due to acoustic-gravity waves, which include both infrasonic and gravity waves, are much larger than the Bragg scale. In order to overcome the large disparity between the scales and be able to explain specular reflections of VHF radar beams, Hocking et al. (1991) and Hocking (2003) proposed that short, highly damped mechanical waves (viscous, thermal, and diffusion waves), which are generated at reflection of long acoustic-gravity waves from sharp, horizontal interfaces within the atmosphere, can create electron density (and, hence, refraction index) inhomogeneities at the radar Bragg scale. Kirkwood et al. (2006) considered the Hocking et al. (1991) hypothesis as a possible mechanism for infrasound generated PMWE. While viscous, thermal, and diffusion waves are well-known in hydrodynamics, their terminology is not fully settled. For example, alternative names for the viscous waves include both "viscosity waves" and "the vorticity mode"; thermal waves are also referred to as "thermal-conduction waves" or "the entropy mode" (see Pierce, 1989; Hocking et al., 1991; Brekhovskikh and Godin, 1998 and the references therein).

One problem with the Hocking hypothesis (Hocking et al., 1991; Hocking, 2003) and its extensions by Kirkwood et al. (2006) is that the atmosphere does not support stationary discontinuities in either temperature, density or wind velocity. Significant, rapid, but continuous changes of the neutral atmospheric parameters on the scale of the VHF wavelength are also not expected to occur in the MLT. Taking into account the results from the previous work (Hocking et al., 1991; Hocking, 2003; Kirkwood et al., 2006; Belova et al., 2020), we consider four possible mechanisms of infrasound-caused specular radar reflection, which do not require sharp interfaces in the MLT: (i) generation of viscous waves at infrasound propagation in a continuously stratified atmosphere; (ii) generation of thermal waves under the same conditions; (iii) direct contributions of infrasound to specular radar reflections; and (iv) generation of thermal waves due to infrasound absorption and/or wave breaking.

A quantitative analysis of these physical mechanisms is outlined in the Appendix. Below, we summarise our findings regarding these models for high-speed PMWE generation.

(i) Viscous waves

Viscous waves are of much shorter wavelength than acoustic waves of the same frequency (in other words, the viscous wave number $k_v = |k_v| exp(i\pi/4)$ is much larger than the acoustic wave number $2\pi f/c$) as long as the attenuation of acoustic waves per wavelength is small (Brekhovskikh and Godin, 1998). Excitation of viscous waves occurs when the acoustic wave propagates in an inhomogeneous fluid. To first order in the small ratio of the acoustic and viscous wavenumbers, the amplitude of the locally generated viscous wave is proportional to the product of the density gradient $\partial\rho_0/\partial z$ and the acoustic pressure. In a horizontally stratified atmosphere, viscous waves have the same horizontal scale and travel horizontally with the same speed as the acoustic waves (sound waves) that caused them. Unlike the sound, the viscous waves do not create mass density perturbations, and the electron density perturbations result from the viscous-wave-induced vertical particle motion. Unless the gradient layer is unrealistically thin (of the order of $1/|k_v|$ or thinner), the viscous wave field and resulting electron density perturbations prove to be much weaker than in the case of a sharp interface with the same overall change in ρ_0.

Hocking et al. (1991), Hocking (2003), and Kirkwood et al. (2006) implied, incorrectly, that the spatial spectrum of monochromatic viscous waves in the atmosphere has a sharp peak where the vertical wavenumber is equal to the real part of k_v, i.e., $2^{-1/2}|k_v|$. In fact, the spectrum of $\partial n/\partial z$ proves to be rather broad, because the viscous waves are strongly evanescent (see the Appendix). It has the width of the order of $|k_v|$ and peaks around $|k_v|$. At MLT altitudes, the spectrum is likely to contain the VHF radar Bragg scale and, hence, efficiently contribute to the coherent radar reflection.

As demonstrated in the Appendix, the existence of a strong density gradient is not sufficient for the viscous waves to create fast-moving coherent radar reflections. Some additional conditions need to be met. These additional conditions are satisfied when the non-zero tail of the atmospheric turbulence spectrum extends into the Bragg scale. Then, the fast-moving radar echoes can be interpreted as the result of the turbulence spectrum being modulated by the viscous waves, which are in turn, generated by and inherit the horizontal structure and horizontal propagation speed of infrasound.

The additional conditions can also be met without turbulence in another scenario, where the strong density gradient $\partial\rho_0/\partial z$ exists in a layer which is thick compared to the viscous wave and the radar wavelength (which are of the order of 1 m), while simultaneously being thinner than the radar range resolution (which is of the order of several hundred metres). Out of these two scenarios, the second one appears to be much more likely to occur.

(ii) Thermal waves

Real atmosphere is not just viscous but also a thermally conducting fluid (Sutherland and Bass, 2004). Thermal waves are generated in parallel with the viscous waves at sound propagation in inhomogeneous, thermally conducting, and viscous fluids. Unlike viscous waves, thermal waves induce mass density oscillations in addition to particle motion. In the atmosphere, the complex wave number of the thermal waves, k_T, is close to that of the viscous waves: $k_T/k_v \approx 0.86$. As for viscous waves, the amplitude of the locally generated thermal waves is proportional to the product of the acoustic pressure and the gradient $\partial\rho_0/\partial z$ of the ambient mass density. In contrast to the viscous waves, the main effect on the gradient $\partial n/\partial z$ of the refraction index arises from the thermal-wave-induced mass density perturbation. The resulting effect of the thermal waves on $\partial n/\partial z$ proves to be much larger than that of the viscous waves (see the Appendix).

The spatial spectrum of $\partial n/\partial z$ has a very broad peak around $2^{-1/2}|k_T|$. Because the peak is so broad, the altitude selectivity for VHF wave reflection does not originate from the thermal waves having exactly the desired Bragg scale. Instead, strong VHF reflections occur around maxima of the absolute value of the product $\Pi = (p/\rho_0^2) N_0\ \partial\rho_0/\partial z$ (see the Appendix), which involves the ambient electron density N_0 in addition to the acoustic pressure p, the ambient mass density ρ_0, and its gradient. The occurrence of thermal-wave-induced coherent radar echoes hence requires that the altitude dependence of this product has a non-zero component at the Bragg scale. As with the viscous waves, the Bragg components in the spectrum of Π may occur due to turbulence or, much more likely, due to the strong mass density gradient occurring in a layer which is thinner than the range resolution of the radar pulse. Alternatively, a large increase in N_0 within a layer with a vertical extent of a few hundred metres would be translated by the thermal waves into coherent radar reflections.

(iii) Direct contributions of infrasound

Acoustic waves modulate the electron density and affect the radio wave refraction index n through wave-induced changes in the mass density and particle motion along the N_0 gradient. These effects are not usually considered in the PMWE context, because the infrasound wavelength is much larger than the VHF radar wavelength, and changes in n are not expected to have an appreciable component at the Bragg scale. The latter reasoning can be questioned, because the altitude dependence of the acoustic pressure is not necessarily sinusoidal. The wave number spectrum is expected to broaden significantly in the vicinity of caustics of acoustic rays, where the acoustic field transitions from interference of two propagating waves on the

insonified side of the caustic to the evanescent wave field on its shadow side (e.g., Brekhovskikh and Godin, 1999). Furthermore, amplification (focusing) of the acoustic field in the caustic vicinity further enhances the direct acoustic effect $\partial n/\partial z$ (Belova et al., 2020). Nevertheless, quantitative estimates show that, at microbarom frequencies and typical values of large-scale temperature gradients, the spectrum broadening and sound amplification fail to produce an appreciable component of the acoustic field (and, hence, $\partial n/\partial z$) at the VHF radar Bragg scale.

In another situation, where strong temperature and mass density gradients exist in the MLT layer, which is thinner than the acoustic wavelength and the radar vertical resolution, sound scattering does produce acoustic field components at the Bragg scale, but the resulting mass density variations and $\partial n/\partial z$ prove to be weaker than the effect of the thermal waves, which are generated by infrasound in the same gradient layer.

(iv) Secondary waves generated as the result of sound dissipation

All three mechanisms discussed so far are contingent on the presence of strong gradients in the atmospheric parameters. During a recent sounding rocket campaign, Strelnikov et al. (2021) observed PMWE occurrences in the regions, where their in-situ measurements did not show any sharp gradients of temperature or mass density. Although high-speed PMWE were neither observed nor specifically addressed by Strelnikov et al. (2021), it is important to point out that infrasound can, in principle, generate high-speed, high-aspect-ratio PMWE even in the absence of the strong gradients. The conceivable mechanism of such generation is associated with infrasound dissipation.

The infrasound dissipation rate grows exponentially with altitude as $1/\rho_0$ and further increases when infrasound propagates against strong winds (Sutherland and Bass, 2004; Godin, 2014). Dissipation of infrasound in the MLT region creates a spatially and temporally modulated heat source, which generates thermal waves. As discussed in the Appendix, these secondary thermal waves inherit the time dependence and horizontal propagation speed of the acoustic wave. The most efficient contribution of the secondary thermal waves into VHF radar pulse reflection is expected to occur when the infrasound dissipation peaks in a relatively thin layer with a vertical extent of ~ 0.5 km or less, e.g., in the vicinity of the ray turning point and/or when the acoustic pressure amplitude approaches the ambient pressure and the acoustic wave approaches breaking.

In summary, the four physical processes, which are discussed above, occur simultaneously and may contribute in various degrees to coherent radar reflections. All mechanisms become more efficient with increasing electron density and acoustic pressure amplitude. The most probable scenario, in which mechanisms (i) - (iii) are efficient in causing radar reflections, also involves a thin layer with thickness of a few hundred metres or less, where strong gradients of the mass density and/or electron density occur.

Among the physical processes we have discussed, infrasound-generated thermal waves appear to be the most probable specific cause of the observed high-speed, high-aspect-ratio PMWE events. With the acoustic pressure due to microbaroms and air temperature at the PMWE generation altitude as well as the vertical dependence of the ambient air density and electron concentration around this altitude as the input data, the mathematical model developed in the Appendix readily provides a quantitative prediction of the radar reflection coefficient due to the thermal waves excited by weakly attenuating infrasound. More detailed information about the acoustic pressure amplitude variation as a function of altitude is required for a quantitative estimation of the contribution of the secondary thermal waves due to the infrasound dissipation.

4. Discussion

Highly aspect sensitive mesospheric echoes travelling with a speed over 300 m/s were observed by ESRAD on several occasions (Kirkwood et al., 2006; Kirkwood 2007). Such measurements are possible due to the configuration of the ESRAD mesospheric experiments and analysis. In the standard FCA (e.g. Holdsworth, 1995), high velocities greater than 250 m/s are automatically rejected as being unrealistic values for wind. We applied all selection criteria to derive FCA true velocity (e.g., Hocking et al., 1989) but did not reject successfully derived high velocity values. For derivation of the horizontal velocity, the FCA method uses cross-correlation of the time series of echoes received by three different antenna subarrays. In order to resolve small time shifts between subarrays i.e. to measure high speeds, the time series should be sampled fast enough. We use short coherent integration times in hardware: about 24 ms in Kirkwood et al. (2006) and 49 ms in this study, and do not apply additional coherent integration for the analysis. Furthermore, in the FCA the vertical radar beam is used that makes it possible to observe (quasi)specular reflection/scattering. For radars using the Doppler Beam Swinging method for derivation of horizontal velocities, highly aspect sensitive echoes ($\theta_s \sim 1°$) will be undetectable with radar beams tilted at 5°-10° or larger angles.

High-speed PMWE are a relatively infrequent phenomenon because their occurrence requires that sufficiently strong infrasound waves (microbaroms) encounter favourable atmospheric conditions. As discussed in Sec. 3 and demonstrated in the Appendix, the atmospheric conditions facilitating PMWE generation are high electron density and neutral temperature gradients and/or wind shear at altitudes reached by microbaroms. The microbaroms generated by nonlinear interaction of surface gravity waves in the North Sea provide strong, albeit intermittent, acoustic waves in the mesosphere above the ESRAD (Landès

et al., 2014). Neither the occurrence of high electron density nor the required neutral atmosphere conditions are in itself exceptional, but their coincidence in space and in time with the independently generated infrasound wave packets is expected to be infrequent.

In order to prove the generation mechanisms proposed in Sec. 3 we need to know parameters describing the infrasonic wave field as well as the state of the neutral and ionised atmosphere, with a high vertical resolution, locally in the mesosphere, i.e. at the place and time of the PMWE events. These data are not available. In-situ atmospheric and plasma measurements have been performed during a limited number of PMWE-dedicated rocket campaigns. However, PMWE moving with high horizontal speed were not registered at these occasions. Moreover, infrasound measurement instrumentation is mainly ground-based, with a limited number of balloon-borne observations (e.g., Bowman and Albert, 2018). Also, it is difficult to measure electron density gradients directly and with a high vertical resolution of a few hundred meters in the lower ionosphere, i.e. at the PMWE altitudes. Therefore, we present here the infrasound observations, microbarom source regions and propagation conditions for three PMWE events shown in Sec. 2, which might support the proposed high-speed PMWE generation hypotheses indirectly. We also discuss ionospheric conditions during these events using satellite observations.

4.1. Microbaroms and infrasound station

As mentioned in the previous sections, microbaroms are infrasound signals originating from nonlinear interactions of ocean surface waves (Brekhovskikh et al., 1973; Waxler et al., 2007; De Carlo et al., 2020). The microbarom frequency ranges typically between 0.1 and 0.35 Hz (Hupe et al., 2019) with a central frequency of 0.2 Hz (Benioff and Gutenberg, 1939). The weak attenuation of low frequencies allows microbaroms to travel over long distances and to be detected by infrasound stations around the globe (Christie and Campus, 2010; De Carlo et al., 2021). In contrast to other infrasound sources (e.g., volcanoes, seismic activity, military explosions), microbaroms are neither localised at a small area, nor stationary. Hence, microbarom signals originating from different ocean regions may simultaneously be detected by an infrasound array.

In this study, data from one ground-based infrasound array, IS37 are analysed. The station IS37 is located in Bardufoss, Norway (69.07° N, 18.61° E) 170 km north-west from ESRAD. The station consists of 10 MB3-type microbarometers and has an aperture of around 2 km (see, e.g., Gibbons et al., 2019). IS37 is a part of the International Monitoring System for verification of the Comprehensive Nuclear-Test-Ban Treaty (Dahlman et al., 2009; Marty, 2019).

Microbaroms detected by the IS37 array have recently been analysed and compared to simulations (Vorobeva et al., 2021; De Carlo et al., 2021), revealing a good agreement between the observed and predicted microbarom fields.

4.2. Vespagrams

For each PMWE event we analyse the microbarom fields recorded by the IS37 arrays during the whole day of the event. This data is analysed on a sliding time window of 1 h, over which the average microbarom-band pressure is estimated every 30 min. This is complemented with a vespagram-based array signal processing analysis (Vorobeva et al., 2021), which shows the directional distribution of the microbarom energy impinging the array for a given apparent velocity.

Fig. 4 displays vespagrams obtained from 0.1 to 0.4 Hz bandpass filtered infrasound recordings at the IS37 station and integrated over apparent velocities above 350 m/s. The apparent velocity is the horizontal velocity with which

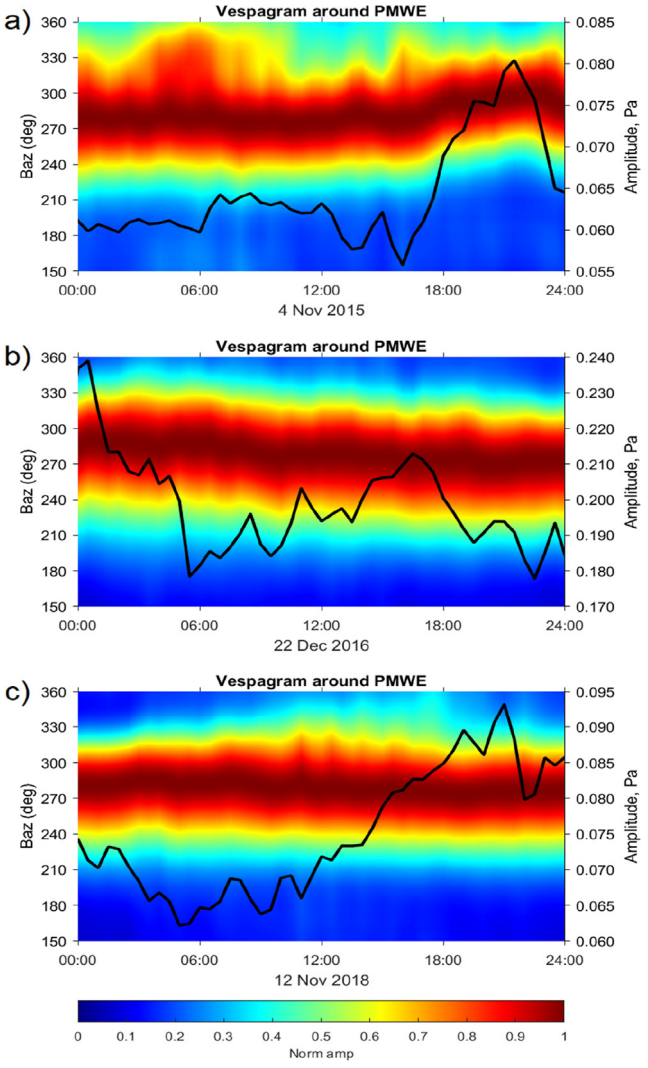

Fig. 4. Colormap - vespagrams for 0.1——0.4 Hz infrasound at IS37 integrated over apparent velocities above 350 m/s and normalised by the maximum amplitude at each time step. Baz is back-azimuth. Black line indicates a maximum microbarom amplitude.

infrasound travels across the array, and can be used as an indicator of the altitude from which the signal is coming. It has been shown in previous studies (Rind et al., 1973; Lonzaga, 2015; Vorobeva et al., 2021) that apparent velocity of 350 m/s corresponds to the higher stratosphere (~50 km). Thus, integration of vespagrams over high apparent velocities provides an estimate of energy coming from 50 km altitude and above (higher stratosphere - mesosphere), where PMWE were observed.

As can be seen in Fig. 4, microbaroms impinging from 270°±20° azimuth are dominating. Based on the IS37 station location, the most likely microbarom source is located in the North Atlantic. The difference in vespagram amplitude suggests that the microbarom source in November 2015 and 2018 was located further away from the infrasound station than in December 2016, and hence, was more attenuated.

4.3. Microbarom source and propagation

In this section, we assess infrasound propagation conditions from the microbarom source location to the infrasound station. We combine models for the microbarom source location and strength with the winds and temperatures of an atmospheric model product.

The microbarom source modelling product used in this study is based on the WAVEWATCH III ocean wave model (The The WAVEWATCH III:® Development Group, 2016, hereafter WWIII). The model output is given on a latitude-longitude grid with 0.5°×0.5° spacing and 3-hour time resolution. One of the WWIII outputs estimates the spectral density of the equivalent surface pressure forcing microbaroms ([dataset] denoted p2l and available via ftp://ftp.ifremer.fr/ifremer/ww3/HINDCAST/SISMO/). This parameter from the time closest to the PMWE event is used as an estimate of microbarom source strength. The pressure-level of the fifth generation ECMWF (ECMWF (2018). reanalysis (ERA5) provides hourly information about atmospheric wind and temperature at 37 levels with 0.25°×0.25° horizontal resolution (Hersbach et al., 2020). In this study, the microbarom oceanic source and the IS37 station are separated by thousands of kilometres. Hence, the presence of a waveguide that is responsible for ducting between the ground and various atmospheric layers is necessary for microbaroms to reach the station. The stratospheric waveguide allows infrasound to travel over longer distances without being strongly attenuated compared to the thermospheric waveguide (Hedlin et al., 2012). For this reason, the effective sound speed c_{eff} (see, e.g., Godin, 2002) is estimated at 1 hPa reanalysis pressure level (~50 km altitude) in order to assess the microbarom propagation conditions towards the IS37 station, $c_{\text{eff}}(z) = 20.05\,T(z) + u_{\perp}(z)$, where T is the atmospheric temperature and $u_{\perp}$ is the projection of the atmospheric wind in the direction to the station. Following Snell's law in a range-independent medium, surface-to-surface refractive ducting conditions are favourable when the effective sound speed increases as a function of altitude above the ground. However, for the lower frequency microbarom regime ducting often occurs for effective sound speed ratios down to ~0.9 (Green and Nippress, 2019; Vergoz et al., 2019). Figs. 5-7 present the geographical maps where the microbarom source amplitude at the sea surface level and the effective sound speed at about 50 km are shown for each of three high-speed PMWE events.

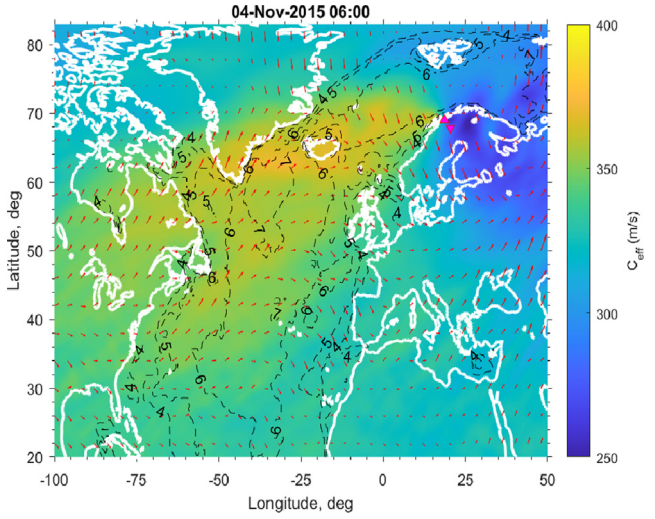

Fig. 5. Colormap shows effective sound speed at the pressure level of 1 hPa based on the ERA5 reanalysis for 4 November 2015, 6:00 UT. Upward-pointing triangle is the station IS37, downward-pointing triangle is the ESRAD site. Black contours are log base 10 of the equivalent surface pressure spectral density from the WWIII model (considered as microbarom source). Red arrows indicate atmospheric wind at the pressure level of 1 hPa predicted by the ERA5 reanalysis.

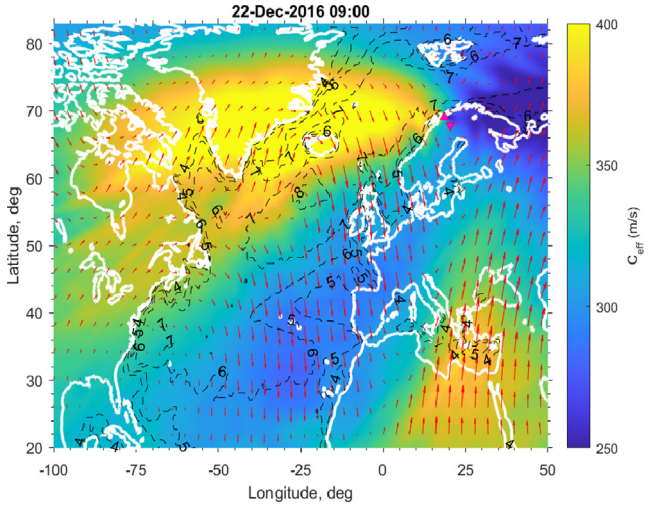

Fig. 6. The same as Fig. 5, but for 22 December 2016, 9:00 UT.

PMWE event 1 (Fig. 5): There is an indication of strong ocean wave activity in the North Atlantic close to Greenland (black dashed contours). The direction to the source corresponds to the one found by the vespagram-based analysis of the infrasound recordings in Fig. 4a. The "hot spot" (strongest ocean activity as presented by black con-

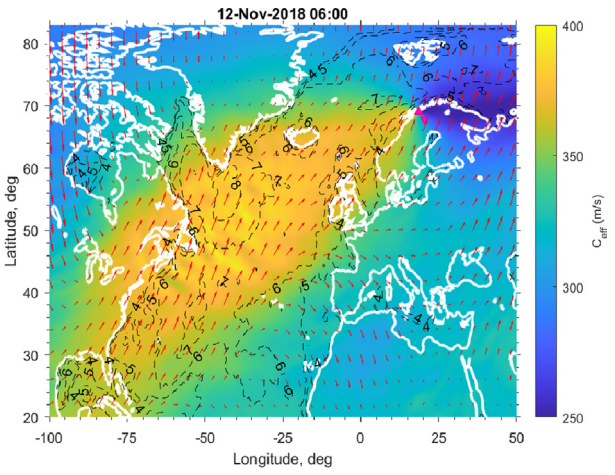

Fig. 7. The same as Fig. 5, but for 12 November 2018, 6:00 UT.

tours) is far away from IS37 station which explains a relatively weak microbarom amplitude. c_{eff} is high above the North Atlantic Ocean, which would support a stratospheric multi-bounce infrasound waveguide. The stratospheric wind direction is favourable and would support microbarom propagation towards the infrasound station and ESRAD site.

PMWE event 2 (Fig. 6): It shows that the microbarom source is stronger and located closer to the IS37 station compared to that on 4 November 2015. This explains higher values of microbarom amplitudes estimated by the vespagram-based approach (Fig. 4b). The effective sound speed at 1 hPa pressure level is highest above Greenland and the North Atlantic and has values up to 400 m/s. This magnitude is sufficient to reflect infrasound and hence, to support stratospheric waveguide. In this case, stratospheric wind is directed near perpendicular to the infrasound propagation (is also called cross-wind). It might cause a difference between microbarom back-azimuth observed at the infrasound station (the vespagram approach) and the real one (Blixt et al., 2019).

PMWE event 3 (Fig. 7): The microbarom source location and strength are similar to 4 November 2015 (Fig. 5). This explains the similarity of microbarom amplitude in the vespagrams. The high c_{eff} values at 1 hPa pressure level above the North Atlantic indicate that stratospheric waveguide is possible. Stratospheric wind is in direction to the station (is also called tail-wind). The presence of a tail-wind, together with high c_{eff} values, would create a waveguide with a very high degree of probability (Blixt et al., 2019).

Further assessment of the microbarom field at the PMWE altitudes and dates may be performed via in-depth wave-propagation analysis using, e.g., parabolic equation-based simulation frameworks. There are expected to be contributions both from MLT ducted microbaroms and from upward leakage of stratospherically ducted microbaroms. This can be a subject for further studies elsewhere.

Regarding experimental evidence of microbarom-related effects at the mesosphere altitudes, it can be noted that Le Du et al. (2020) detected microbarom signatures at 87 km altitude using OH airglow observations above the Haute-Provence Observatory, France.

4.4. Ionospheric conditions

In Sec. 2.3, the observations of the solar wind speed made onboard of GOES satellites and cosmic noise absorption made by the ground-based riometers in Kiruna were described for each of the PMWE events. All three events were characterised by action of the high-speed solar wind streams on the Earth's atmosphere that resulted in energetic electron precipitation from the magnetosphere. This, in turn, leads to increased ionisation in the ionospheric D-region, i.e. at the PMWE altitudes as indicated by the enhanced cosmic noise absorption measured by the riometers. The PMWE event on 4 November 2015 is characterised by stronger D-region ionisation than two other PMWE events. Very high cosmic noise absorption of 6 dB that was measured by the Kiruna riometer on 4 November 2015 is a sign of this ionisation.

4.5. Assessment of generation mechanisms

As pointed out in the summary of Sec. 3, all proposed mechanisms work more effectively with increasing electron density and infrasound signal amplitude at the point of PMWE generation. We found that at the time of the selected PMWE events the infrasound waves generated by the sources located in the North Atlantic could reach mesospheric heights above ESRAD due to effective ducting. In the absence of in-situ infrasound measurements, the maximum of the microbarom amplitude with apparent velocity of more than 350 m/s at IS37 is used to make an assumption of the acoustic signal strength at mesospheric heights. The infrasound data used in this study were obtained from IS37 which is located about 170 km from the ESRAD site. This distance is much shorter than the distance between the ESRAD site and the microbarom source (see Figs. 5-7). Thus, we do not expect any substantial difference between the microbarom signals at these two sites. For the second event the microbarom amplitude was about 3 times higher than for two others, however, the PMWE were more powerful for the first event, probably because the electron density was strongly enhanced.

We can conclude that during all three PMWE events the local atmospheric and plasma conditions were favourable for hypothetical enabling of all four physical mechanisms discussed in Sec. 3. These conditions include: (1) strong (in terms of amplitude) microbarom source, (2) atmospheric conditions facilitating infrasound propagation toward the radar site, (3) successful microbarom detection at the ground station located relatively close to the radar, and (4) the enhanced electron density (and possibly, increased gradients of electron density) at the PMWE altitudes. Infrasound-generated thermal waves are the most probable specific cause of the observed high-speed and

high-aspect-ratio PMWE events. However, the limited experimental data do not allow us to offer a detailed, quantitative assessment of efficiency of various physical mechanisms considered in Sec. 3 in the process of high-speed PMWE generation during the selected events. We have no direct experimental evidence for existence of thin layers where strong gradients in the neutral atmosphere and/or electron density occur. Nevertheless, in all three cases energetic electron precipitation occurred which could have caused such layers in the electron density.

5. Conclusions

In this paper we considered three PMWE events measured by the MST radar ESRAD located near Kiruna in northern Sweden. These events were characterised by shorter periods when the echoes had high horizontal velocities above 300 m/s. During these PMWE events, the Earth atmosphere was also affected by the high-speed solar wind streams, and strong ionospheric disturbances were registered by riometers at Kiruna. In order to explain the extraordinarily large horizontal velocities during these echoes, we proposed four mechanisms involving microbaroms i.e. infrasound waves at 0.1–0.35 Hz frequencies originating from ocean swell. These mechanisms include (i) generation of viscous waves, (ii) generation of thermal waves, (iii) direct contributions of infrasound, and (iv) generation of secondary waves at sound dissipation. All four mechanisms can simultaneously contribute to the high-speed PMWE generation. Under certain conditions in the neutral atmosphere and plasma in the region of mesospheric echo generation, some mechanisms can be more efficient than others. For instance, from the theoretical considerations we expect that infrasound-generated thermal waves are the most probable cause of the high-speed PMWE. For assessment of the proposed mechanisms, we analysed the infrasound signals detected at IS37 station located at about 170 km north-west from Kiruna, together with the modelled maps of the microbarom sources and the effective sound speed at 50 km altitude. Since we used microbarom propagation in the stratosphere as a proxy, due to absence of mesospheric in-situ infrasound data, we might also expect contributions of microbarom leakage from the stratospheric waveguide and of MLT ducted modes. We conclude that for all three PMWE events, atmospheric conditions favoured propagation of microbaroms originating in the North Atlantic to IS37 and Kiruna via effective stratospheric ducts and that the microbarom amplitudes were likely to be sufficient for generation of the observed high-speed PMWE.

Declaration of Competing Interest

The authors declare that they have no known competing financial interests or personal relationships that could have appeared to influence the work reported in this paper.

Acknowledgments

ESRAD operation and maintenance is provided by the Esrange Space Center of the Swedish Space Corporation (SSC).

We acknowledge partial support from the project Middle Atmosphere Dynamics: Exploiting Infrasound Using a Multidisciplinary Approach at High Latitudes (MADEIRA), funded by the Research Council of Norway basic research programme FRIPRO/FRINATEK under Contract No. 274377.

Evgenia Belova thanks Sheila Kirkwood for the fruitful discussions and help with the ESRAD data analysis.

Appendix. Model of generation of High-Speed PMWE by infrasound

Here we outline the quantitative analysis of four possible physical mechanisms of PMWE generation by infrasound in a continuously stratified MLT, which are discussed in Sec.3.

A.1. Radar scattering due to mechanical waves in the MLT

Acoustic waves introduce time-dependent changes in pressure, temperature, and the fluid (air) density and are accompanied by oscillatory motion of fluid parcels. These perturbations of the ambient state are reflected in the electron density.

Assuming for simplicity that the atmosphere remains neutral during passage of an acoustic wave (i.e., electrons follow ions and move with neutral component of the atmosphere) and disregarding all ionisation and recombination processes, electron density N (i.e., the number of electrons per unit volume) satisfies the equation

$$\frac{\partial N}{\partial t} + \nabla \cdot (N\boldsymbol{V}) = 0. \tag{A1}$$

Here t stands for time, $\boldsymbol{V} = \boldsymbol{v} + \boldsymbol{u}$ is the fluid parcel velocity, which is the sum of the wind velocity $\boldsymbol{u}$ and the oscillatory velocity $\boldsymbol{v}$ due to waves. Eq. (A1) expresses conservation of the total number of electrons and coincides with the usual equation for the density of advected admixtures (passive tracers) (Brekhovskikh and Godin, 1999).

In a homogeneous atmosphere with uniform electron density and no wind, $N/N_0 = \rho/\rho_0$, where ρ is mass density and subscript *0* refers to ambient (unperturbed) values of respective physical quantities. The relation between wave-induced perturbations $N_1 = N - N_0$ and $\rho_1 = \rho - \rho_0$ in the electron and mass density is more involved in the actual, inhomogeneous atmosphere. For waves with the harmonic dependence $\exp(i\boldsymbol{k}\dot{s}\boldsymbol{r} - i\omega t)$ on horizontal coordinates and time, linearization of Eq. (A1) with respect to the wave amplitude gives:

$$\frac{N_1}{N_0} = \frac{\rho_1}{\rho_0} + \frac{iv_3}{\omega - \boldsymbol{k}\cdot\boldsymbol{u}}\left(\frac{1}{\rho_0}\frac{\partial \rho_0}{\partial z} - \frac{1}{N_0}\frac{\partial N_0}{\partial z}\right). \tag{A2}$$

Here $\boldsymbol{r} = (x, y, z)$ and $\boldsymbol{k} = (k_1, k_2, 0)$ are the position vector and horizontal wave vector; x, y, and z are Cartesian coordinates with the vertical coordinate z increasing upwards; $\boldsymbol{v} = (v_1, v_2, v_3)$. It is assumed in Eq. (A2), that the wind velocity is horizontal and physical parameters of the ambient (unperturbed) atmosphere depend only on z. Eq. (A2) shows that, in addition to mass density variations, first-order changes in the electron density are caused by the wave-induced oscillatory displacement of fluid parcels in the direction of variation of the ambient electron density N_0. Depending on the value of $\partial N_0/\partial z$, the term with v_3 may dominate in the right side of Eq. (A2). This is particularly important for the waves, such as viscous waves, in which mass density perturbation ρ_1 is negligible.

Specular reflection of a radar beam occurs when it encounters inhomogeneities of the electromagnetic wave refraction index n, that are coherent in two transverse dimensions to the beam at horizontal ranges larger than a Fresnel zone. Gage and Balsley (1980) refer to such a reflection as a Fresnel reflection. The Fresnel zone radius is of the order of a few kilometres for the radars and PMWE altitudes for the observations described in Sec. 2. The condition of the coherent electron density and, hence, refraction index variations over such scales are met for perturbations of horizontally stratified ambient atmosphere due to microbaroms that propagate to the radar vicinity from distant sources.

For the electromagnetic wave reflection coefficient of a radar beam with the range resolution Δr from the altitude H, Gage and Balsley (1980) use the equation

$$R = \frac{1}{4}\left|\int_{H-\Delta r/2}^{H+\Delta r/2} F\frac{\partial n}{\partial z}\exp\left(\frac{4i\pi z}{\lambda_R}\right)dz\right|^2 \tag{A3}$$

with $F = 1$, where λ_R is the radar wavelength. The radar beam is assumed to be vertical. At the altitudes of interest in the PWME problem

$$\nabla n = -(2N_c)^{-1}\nabla N, \tag{A4}$$

where $N(\boldsymbol{r})$ and N_c are the electron density and the critical plasma density, respectively. N_c (in m^{-3}) is related to the radar frequency f_R (in MHz) by $N_c = 1.24\cdot 10^{-2} f_R^2$ (Gage and Balsley, 1980).

Reflections of different strengths, or no reflections at all, are returned from different altitudes H depending on the magnitude and spectrum of $\partial n/\partial z$ at $H - \Delta r/2 < z < H + \Delta r/2$. If $\partial n/\partial z = 0$ outside of this interval, R is proportional to the value of the one-dimensional spatial spectrum of the refraction index gradient evaluated at the Bragg wavenumber equal twice the wavenumber of the electromagnetic wave. It is important to note that, however, even when $\partial n/\partial z$ is constant and, hence, has zero spectrum level at the Bragg wavenumber, Eq. (A3) (with $F = 1$) gives non-negligible values of R on the order of $R \sim 0.5(4\pi)^{-2}(\lambda_R \partial n/\partial z)^2$ (unless the ratio $\Delta r/\lambda_R$ is an integer).

Eq. (A3) with $F = 1$ is just the Born approximation for electromagnetic wave reflection from a continuously stratified layered medium (see, e.g., Brekhovskikh and Godin, 1998). It implies that the incident wave intensity is constant within the 'box-car' radar pulse (i.e., at $H - \Delta r/2 < z < H + \Delta r/2$) and is zero outside, which is an idealisation. The factor F is included in Eq. (A3) to account for the pulse shape. A smooth pulse shape that gradually goes to zero with increasing $|z - H|$ can significantly decrease R when the spectrum of $\partial n/\partial z$ does not include components at or around the Bragg wavenumber. For typical values of $\Delta r/\lambda_R \gg 1$, the magnitude of the decrease is dramatically different for pulses with the Gaussian and trapezoidal shapes.

A.2. Generation of viscous waves by an acoustic wave in a continuously stratified fluid

Here we consider an inhomogeneous viscous fluid and, for now, disregard its thermal conductivity. Acoustic and viscous waves do not interact in homogeneous, unbounded viscous fluids, but become coupled at boundaries and interfaces as well as by gradients of the fluid's parameters (density ρ_o, sound speed c, and shear viscosity η) (Pierce, 1989; Brekhovskikh and Godin, 1998). When an acoustic wave is incident on a boundary or interface or propagates through an inhomogeneous layer, viscous waves are generated due to the coupling. The coupling has been previously considered at a boundary of a homogeneous fluid and at an interface of two homogeneous fluids (Savel'ev, 1973; Pierce, 1989; Brekhovskikh and Godin, 1998). To extend the theory to coupling in continuously varying fluid, we take advantage of the known fact that, in the absence of wind, linear wave propagation of monochromatic waves in a viscous fluid is mathematically equivalent to wave propagation in a solid with shear modulus $\mu = -i\omega\eta$, where ω is the wave frequency (Brekhovskikh and Godin, 1998). Then, the viscous waves are the corresponding shear waves with the complex wave number

$$k_v = \omega\sqrt{\frac{\rho_0}{\mu}} = (1+i)\sqrt{\frac{\omega\rho_0}{2\eta}}. \tag{A5}$$

In the atmosphere, $|k_v|$ decreases exponentially with altitude because of the density variation. At the altitudes of interest in the PMWE problem, infrasound attenuation per wavelength is small, $|k_v| \gg \omega/c$, and, therefore, viscosity and equivalent shear rigidity are also small in the following sense: $|\mu| = \omega\,\eta \ll \rho_0 c^2$. Note that, unlike acoustic waves, the density changes in viscous waves are negligible and are exactly zero in homogeneous fluids, just as in the shear waves in homogeneous solids.

Consider a horizontally stratified viscous fluid, parameters of which depend only on the altitude z. Acoustic waves with the harmonic dependence $\exp(i\boldsymbol{k}\cdot\boldsymbol{r} - i\omega t)$, $\boldsymbol{k} = (k, 0, 0)$ on horizontal coordinates and time will generate viscous waves with the same dependence on x, y, and t. Our goal here is to relate the amplitude of the viscous waves to gradients of the atmospheric parameters. Let the ambient parameters of the fluid vary on a spatial scale

that is large compared to $1/|k_v|$ in a thick "gradient layer." We first approximate the gradient layer by a sequence of small jumps in the ambient parameters $\rho_o(z)$, $c(z)$, and $\eta(z)$ at $z = z_j$, $j = 1, 2, \ldots$. The jumps (interfaces) are separated by a distance large compared to $1/|k_v|$, so that the viscous waves generated at one interface attenuate and do not reach another interface. Parameters of the fluid are constant in every thin layer between two adjacent interfaces.

The problem of conversion of compressional to shear waves in a discreetly stratified solid with weak shear rigidity was recently studied by Godin (2021). Taking advantage of the mathematical equivalence between shear waves in solids and viscous waves in fluids, we find that an acoustic wave will generate a viscous wave with fluid parcel velocities $\boldsymbol{v} = (v_1, 0, v_3)$

$$v_1 = \frac{(z-z_j)\beta}{|z-z_j|k} v_3, \quad v_3 = -\frac{k^2 p}{2\omega k_v \rho_0^2}\rho_{0j}\exp\left(i\beta|z-z_j|\right), \quad \beta = \sqrt{k_v^2 - k^2}, \tag{A6}$$

at the jth interface. Here and below the dependence $\exp(i\boldsymbol{k}\cdot\boldsymbol{r} - i\omega t) = \exp(ikx - i\omega t)$ on horizontal coordinates and time is implied and suppressed for brevity; the branch of the square root is chosen so that the imaginary part is non-negative: $Im\sqrt{k_v^2 - k^2} \geqslant 0$. In Eq. (A6), p stands for the acoustic pressure in the sound wave at $z = z_j$, and $\rho_{0j} = \rho_0(z_j + 0) - \rho_0(z_j - 0)$ is the jump of density across the interface. Importantly, the sound wave can be any combination of the acoustic waves travelling up and down or evanescent, but with the same horizontal wave vector $\mathbf{k}$. In Eq. (A6), we retained only the terms of the first order with respect to (i) the small jumps of the ambient parameters across the interface, and to (ii) the small parameter $|k_v|^{-1}\omega/c \ll 1$. According to Eq. (A6), the fluid motion in the viscous wave is nearly horizontal since $|\beta| \approx |k_v| \gg |k|$, regardless of the direction of sound propagation. The first-order contributions to the viscous wave generation are due to ambient density jump across the interface, while jumps in the sound speed or viscosity do not give any first-order contributions. Although not considered here, additional contributions to the viscous wave generation are expected to result from the wind shear, i.e., from variations of the wind velocity with z.

The combined effect of all the interfaces is given by the sum of contributions in Eq. (A6):

$$v_1(z) = \frac{1}{ik}\frac{\partial v_3}{\partial z}, \quad v_3(z) = -\frac{k^2}{2\omega}\sum_j \frac{p}{k_v\rho_0^2}\rho_{0j}\exp\left(i\beta|z-z_j|\right). \tag{A7}$$

The sum in the right side of Eq. (A7) is a discrete approximation of an integral over dz_j and reduces to the integral in the limit of the infinite number of the interfaces:

$$v_1(z) = \frac{1}{ik}\frac{\partial v_3}{\partial z}, \quad v_3(z) = -\frac{k^2}{2\omega}\int \frac{p}{k_v\rho_0^2}\frac{\partial \rho_0}{\partial z_0}\exp\left(i\beta|z-z_0|\right)dz_0, \tag{A8}$$

where the integration extends through the entire gradient layer. Eq. (A8) gives the dominant term of the asymptotic solution of the problem of the viscous wave generation in the continuously stratified fluid. As expected, the solution is independent of the arbitrary choice of positions of the auxiliary interfaces $z = z_j$.

From Eq. (A2) we find:

$$N_1 = \frac{iv_3 N_0}{\omega}\left(\frac{1}{\rho_0}\frac{\partial \rho_0}{\partial z} - \frac{1}{N_0}\frac{\partial N_0}{\partial z}\right) \tag{A9}$$

for the electron density perturbation due to the viscous waves. In the case of a single, sharp interface at $z = z_1$, the spatial Fourier spectrum $\tilde{n'}_z(\mu)$ of the derivative $\partial n/\partial z$ of the refraction index in Eq. (A3) has a peak around $\mu = |\beta| \approx |k_v|$. Indeed, from Eq. (A4), (A6) and (A)9 we find:

$$\tilde{n'}_z(\mu) = \frac{i\mu}{2N_e\omega}\tilde{N}_1(\mu) \approx \frac{-\mu}{2N_e\omega}\left(\frac{N_0}{\rho_0}\frac{\partial \rho_0}{\partial z} - \frac{\partial N_0}{\partial z}\right)\Big|_{z=z_1}\tilde{v}_3(\mu), \tag{A10}$$

$$\tilde{v}_3(\mu) = \frac{1}{2\pi}\int_{-\infty}^{\infty} e^{-i\mu z}v_3 dz = \frac{ik^2 p}{2\pi\omega k_v\rho_0^2}\Big|_{z=z_1} e^{-i\mu z_1}\frac{\rho_{01}\beta(z_1)}{\mu^2 - \beta^2(z_1)}. \tag{A11}$$

According to Eq. (A10) and (A11), the dependence of $\tilde{n'}_z(\mu)$ on the spectral parameter α is given by the factor B:

$$B(\mu) = e^{-i\alpha z_1}\frac{\mu\beta(z_1)}{\mu^2 - \beta^2(z_1)}. \tag{A12}$$

Recall that β is complex and close to k_v according to Eqs. (A5) and (A6), while μ is real-valued. Hence, B is always finite; $B \sim 1$ when $|\mu/\beta| \sim 1$, and $B = 0$ when either $\mu = 0$ or $\alpha|\to\infty$. The absolute value of B and, hence, of the spectrum of $\partial n/\partial z$ is maximum at $\mu = \pm\mu_m$,

$$\mu_m = \left(|k_v^4| + k^4\right)^{1/4} \approx |k_v| = \sqrt{\omega\rho_0/\eta}. \tag{A13}$$

Note that, unlike the case of real β, the spectral peaks are not very sharp when $Im\,\beta \approx Re\,\beta$. However, the contrast between the spectral values at $\mu = \pm\mu_m$ and at $|\mu| \ll |\beta|$ or $|\mu| \gg |\beta|$ is very large. Hocking et al. (1991), Hocking (2003) and Kirkwood et al. (2006) argued that these spectral peaks lead to specular radar reflection from the altitudes, where $\mu_m = 4\pi/\lambda_R$. (Based on qualitative arguments, Hocking et al. (1991), Hocking (2003) and Kirkwood et al. (2006) implied, incorrectly, that $\mu_m = Rek_v = 2^{-1/2}|k_v|$.).

As in the case of a sharp interface, the presence of the factor $\exp(i\beta|z - z_0|)$ in the integrand in Eq. (A8) has a

similar effect on the spectra of N_1 and $\partial n/\partial z$, when the viscous waves are generated in a gradually stratified atmosphere. It is easiest to see in the case, when $N_0\rho_0^{-1}\partial\rho_0/\partial z - \partial N_0/\partial z$ and k_v vary little and can be assumed constant either in the range of altitudes, where the viscous waves are generated, or within the vertical resolution range $H - \Delta r/2 < z < H + \Delta r/2$ of the radar. Then, Eq. (A10) remains valid, with z_1 being an arbitrary point within, respectively, the viscous wave generation layer or the resolution range. For the v_3 spectrum, from Eq. (A8) we find:

$$\tilde{v}_3(\mu) = \frac{ik^2\beta}{\omega k_v(\mu^2-\beta^2)}\bigg|_{z=z_1} e^{-i\mu z_1} D(\mu),$$
$$D(\mu) = \int_{-\infty}^{\infty} e^{-i\mu(z-z_1)} \frac{\partial\rho_0}{\partial z_0}\frac{pdz}{2\pi\rho_0^2}, \qquad \text{(A14)}$$

where $D(\mu)$ is proportional to the spectrum of $p\rho_0^{-2}\partial\rho_0/\partial z$. Eq. (A14) is similar to Eq. (A11). Assuming that $D(\mu)$ has no scales of the order of $|k_v|$, the dependence $D(\mu)$ is reasonably flat in the vicinity of $\mu = \pm\mu_m$. As long as the spectrum of $p\rho_0^{-2}\partial\rho_0/\partial z$ is nonzero in the vicinity of $\mu = \pm\mu_m$, it follows from Eq. (A10) and (A14) that the dependence of the spectrum $\tilde{n'}_z(\mu)$ of $\partial n/\partial z$ on μ is again given approximately by $B(\mu)$ in Eq. (A12) and, therefore, is expected to have the same peaks as in the case of a sharp interface.

Aside from the large-wavenumber components of the spectrum being artificially generated by the finite range resolution, as discussed in Sec. A.1, there are at least two situations, when $D(\mu)$ is nonzero in the vicinity of $\mu = \pm\mu_m$ regardless of the pulse shape of the radar pulse. First, the spectral components around $\mu = \pm\mu_m$ may represent atmospheric turbulence, perhaps a tail of the turbulence spectrum. Then, the fast-moving coherent echoes are a combined result of the atmospheric turbulence and the viscous waves, the latter being generated by infrasound. Second, the needed spectral components of $D(\mu)$ arise, when the strong gradient $\partial\rho_0/\partial z$ of the density exists in a layer, which is thick compared to viscous wave and radar wavelengths but smaller than the range resolution $2\Delta r$ in Eq. (A3). Of these two scenarios, the second situation appears to be a likelier mechanism of producing detectable amplitudes of the coherent radar reflections.

A.3. Generation of thermal waves by an acoustic wave in a continuously stratified fluid

In addition to acoustic and viscous waves, mechanical waves in fluids include thermal waves, or the "entropy mode." The thermal waves arise due to finite, non-zero thermal conductivity of the fluid. In the regime of "weak" viscosity and thermal conductivity, when absorption of sound is small over ranges of the order of the acoustic wavelength, the wavenumber of thermal waves is (Pierce, 1989; Brekhovskikh and Godin, 1998)

$$k_T = (1+i)\sqrt{\frac{\omega\rho_0 C_p}{2\kappa}}, \qquad \text{(A15)}$$

where κ are C_p are the thermal conductivity and specific heat at constant pressure. The thermal waves are rapidly attenuating ones. The wavenumber of thermal waves is complex and, just as for viscous waves, has equal real and imaginary parts, which are much larger than the acoustic wavenumber: $Rek_T = Imk_T \gg \omega/c$. Kinematically, thermal and viscous waves are very similar. Moreover, $|k_v|$ and $|k_T|$ have comparable values in the atmosphere, regardless of the altitude and wave frequency. Indeed, Eq. (A5) and (A15) give

$$\frac{k_T}{k_v} = \sqrt{\mathrm{Pr}}, \quad \mathrm{Pr} = \frac{\eta C_p}{\kappa} \qquad \text{(A16)}$$

in terms of the Prandtl number Pr. The Prandtl number is nearly constant in the atmosphere, and to a good accuracy $Pr = 4\gamma/(9\gamma - 5)$, where γ is the ratio of specific heats at constant pressure and constant volume (Sutherland and Bass, 2004). With $\gamma = 1.4$ we have $Pr = 14/19$ and $k_T/k_v \approx 0.86$.

Unlike the viscous waves, propagation of thermal waves is accompanied by mass density variations and, therefore, can lead to electron density perturbations in a homogeneous atmospheric layer with constant electron density. Oscillatory velocity of fluid parcels in a monochromatic thermal wave is related to the pressure perturbation p by the same relation as for acoustic waves, while the density perturbation for a given p is much larger than in acoustic waves (Brekhovskikh and Godin, 1998):

$$\boldsymbol{v} = \frac{\nabla p}{i\omega\rho_0}, \quad \rho_1 = \frac{k_T^2}{\omega^2}p. \qquad \text{(A17)}$$

When viscosity and thermal conductivity are both weak, excitation of viscous and thermal waves by an acoustic wave can be considered separately. Excitation of viscous waves in a fluid with a negligible thermal conductivity is considered in Sec. A.2. Here we consider reflection and, more generally, propagation of acoustic waves in an inviscid, thermally conducting fluid. At an interface in a thermally conducting fluid, waves must satisfy the boundary conditions of continuity of pressure, temperature, normal component of the oscillatory, or fluid parcel, velocity, and normal (to the interface) component of the heat flux (Brekhovskikh and Godin, 1998). Let a plane acoustic wave with the dependence $\exp(i\boldsymbol{k}\cdot\boldsymbol{r} - i\omega t) = \exp(ikx - i\omega t)$ on horizontal coordinates and time be incident from below on the horizontal interface $z = z_0$ of two homogeneous fluids. Parameters of the fluids below and above the interface will be distinguished by using the subscripts 1 and 2, respectively. The pressure perturbations due to acoustic and thermal waves are given by the expressions

$$p = p_{in}[\exp(i\alpha_1(z-z_0)) + V_a\exp(i\alpha_1(z_0-z)) + V_T\exp(i\beta_1(z_0-z))],$$
$$\beta_1 = \sqrt{k_{T1}^2 - k^2}, \quad z < z_0; \qquad \text{(A18)}$$

$$p = p_{in}[W_a \exp(i\alpha_2(z - z_0)) + W_T \exp(i\beta_2(z - z_0))],$$
$$\beta_2 = \sqrt{k_{T2}^2 - k^2}, \quad z > z_0. \tag{A19}$$

The common factor $\exp(ikx - i\omega t)$ is suppressed for brevity. In Eq. (A18) and (A19), $\alpha_{1,\,2}$ and $\beta_{1,\,2}$ stand for the vertical components of the acoustic and thermal wave vectors in respective fluids; p_{in} has the meaning of the complex amplitude of the incident wave at $z = z_0$.

The reflection V_a and transmission W_a coefficients of the acoustic wave as well as the complex amplitudes V_T and W_T of the thermal waves in each of the fluids are found by imposing the above-stated boundary conditions. The exact expressions are cumbersome, and we present here only approximate results for the thermal wave amplitudes, which are valid to first order in the relative variations of the thermal conductivity, mass density, and sound speed across the interface:

$$V_T = -W_T = \frac{(\gamma - 1)\omega^2 S}{2k_T^2 c^2}, \tag{A20}$$

$$S = \frac{\gamma_1 p_{01} C_{p2} \rho_{02}^2 c_2^2}{\gamma_2 p_{02} C_{p1} \rho_{01}^2 c_1^2} - 1. \tag{A21}$$

The quantities k_T, γ, c without subscripts refer to the average of the respective parameters on the opposite sides of the interface. Only the dominant-order terms in the small parameter $|\omega/ck_T| \ll 1$ are retained in Eq. (A20). From Eq. (A17)–(A20) we find

$$\frac{\partial \rho_1}{\partial z} = \frac{i(\gamma - 1)k_T}{2c^2} p_{in} S e^{ik_T|z - z_0|} \tag{A22}$$

for the density perturbation due to the thermal waves. This result is similar to Eq. (A6) for the vertical velocity due to viscous waves at reflection from a sharp interface. Eq. (A22) does not contain α or k and, therefore, applies to reflection of an arbitrary acoustic wave, which can include upward- and downward-propagating components.

In the particular case of the fluid being an ideal gas of constant composition, Eq. (A21) simplifies and S reduces to the relative change in mass density across the interface. The thermal waves in Eq. (A22) create perturbations in the electron density even when its gradients are negligible. From Eq. (A2), (A4) and (A22) we find

$$\frac{\partial n}{\partial z} = -\frac{iN_0(\gamma - 1)k_T \delta\rho_0}{4N_e \rho_0^2 c^2} p_{in} e^{ik_T|z - z_0|} \tag{A23}$$

for the gradient of the refraction index of radio waves. The amplitude of the refraction index gradient caused by the thermal waves differs by the factor $\left|k_T N_0 (\partial N_0/\partial z)^{-1}\right| \gg 1$ from the gradient caused by viscous waves (Sec. A.2). Hence, the effect of thermal waves is orders of magnitude larger than the effect of viscous waves at infrasound reflection from a sharp interface.

Generation of the thermal waves at sound propagation through a continuously stratified fluid can be considered by approximating the continuous stratification by a series of discontinuous variation across a large number of horizontal interfaces. Quite analogously to derivation of Eq. (A8) in Sec. A.2, from Eq. (A22) and (A23) we find

$$\frac{\partial \rho_1}{\partial z} = \frac{i(\gamma - 1)}{2} \int \frac{k_T p}{\rho_0 c^2} \frac{\partial \rho_0}{\partial z_0} e^{ik_T|z - z_0|} dz_0, \tag{A24}$$

$$\frac{\partial n}{\partial z} = -\frac{i(\gamma - 1)}{4N_e} \int \frac{k_T p}{\rho_0^2 c^2} \frac{\partial \rho_0}{\partial z_0} N_0 e^{ik_T|z - z_0|} dz_0 \tag{A25}$$

for the effect of the thermal waves. In Eq. (A24) and (A25), p is the acoustic pressure in the infrasonic wave.

The spatial spectrum of $\partial n/\partial z$ can be calculated just as in Sec. A.2. The spectrum peaks around $\pm Rek_T$. These peaks are large but very wide. They are even wider, than in the case of viscous waves. This means that the altitude selectivity for electromagnetic wave reflection originates not from the thermal waves having exactly the desired Bragg scale but from the altitude dependence of the product $(p/\rho_0^2) N_0 \partial\rho_0/\partial z$ in the integrand in Eq. (A25). Much like in the case of viscous waves, the occurrence of coherent radar echoes because of the thermal waves requires that the altitude dependence of $(p/\rho_0^2) N_0 \partial\rho_0/\partial z$ within the altitude range $H - \Delta r < z < H + \Delta r$ has a non-zero component at the Bragg scale. Then, according to Eq. (A25), the amplitude of the Bragg component in $\partial n/\partial z$ is enhanced by the thermal waves. As discussed in Sec. A.2 in the context of the radar scattering facilitated by the viscous waves, the Bragg components in the spectrum of $(p/\rho_0^2) N_0 \partial\rho_0/\partial z$ may occur due to turbulence or, more likely, from the significant density gradient $\partial\rho_0/\partial z$ occurring in a layer that is thinner than the range resolution of the radar pulse.

A.4. Direct contributions of infrasound to specular radar reflections

The physical mechanisms of the radar reflection discussed so far involved short, evanescent waves generated by infrasound at propagation through layers with large temperature gradients in the atmosphere. The direct contributions of infrasound to the electromagnetic wave reflection coefficient R in Eq. (A3) are not normally considered, because the infrasound wavelength is much longer than the radar wavelength, and the acoustic field is not supposed to have any spectral components at the Bragg wavenumber.

The above reasoning is largely but not entirely correct because, first, dependence of the acoustic field on altitude is not necessarily sinusoidal, and second, the integral in the right side of Eq. (A3) is taken over a finite altitude range sinusoidal, and third, the integral in the right side of Eq. (A3) is taken over a finite altitude range $H - \Delta r/2 < z < H + \Delta r/2$. As discussed in Sec. A.1, R may have non-negligible values even when $\partial n/\partial z =$ constant at $H - \Delta r/2 < z < H + \Delta r/2$.

The largest direct contributions of acoustic waves to radar specular reflection are expected to occur, when (i) rel-

ative density perturbations and/or oscillatory velocity in the acoustic wave are large, and (ii) the acoustic wave is not sinusoidal, and its altitude dependence has a broad wavenumber spectrum. These conditions are met simultaneously in the vicinity of turning points and caustics of infrasound waves in MLT. Wave amplitude is known to increase around the caustics, where the nature of the field changes from interference of the direct and caustic-reflected propagating waves on the insonified side of the caustic to the field being an evanescent wave (in the direction normal to the caustic) in the "shadow zone" behind the caustic (Brekhovskikh and Godin, 1999).

However, quantitative estimates show that, in the microbarom frequency range and in the absence of strong temperature and wind velocity gradients, amplitude and phase variations in the acoustic field, even in the vicinity of caustics, occur too gradually to change the contribution to the radio wave reflection coefficient, Eq. (A3), compared to the case of constant $\partial n/\partial z$. As discussed in Sec. A.1, the latter contribution strongly depends on the radar pulse shape and becomes negligibly small for the Gaussian pulse.

Acoustic wave acquires a component that varies rapidly with altitude, when the wave propagates through strong gradients of the density, sound speed or wind velocity. If the strong gradient occurs in a layer $z_1 - h < z < z_1 + h$, which is thin compared to the acoustic wavelength, rapid variations of the sound field occur only within the layer (Brekhovskikh and Godin, 1998) and are due to reflection (scattering) of sound by small-scale inhomogeneities. Acoustic field within the layer can be found by replacing the gradient by a sequence of small jumps, as was illustrated for the viscous and thermal waves in Sections A.2 and A.3. Calculation of V_a and W_a in Eq. (A18) and (A19) shows that sound scattering by strong gradients results in a contribution to the radar reflection coefficient in Eq. (A3), which is independent of the radar pulse shape. However, the effect of sound scattering on $\partial\rho_1/\partial z$ and $\partial n/\partial z$ proves to be weaker than the effect of the simultaneously generated thermal waves. For a temperature gradient occurring in the layer $z_1 - h < z < z_1 + h$ located within the altitude range $H - \Delta r/2 < z < H + \Delta r/2$ in Eq. (A3), sound scattering gives the radar reflection coefficient that is smaller by the factor of the order of $|\alpha h|^{-2} \gg 1$ than the radar reflection due to the thermal waves. Here, $\alpha = \left(\omega^2 c^{-2} - k^2\right)^{1/2}$ is the vertical component of the wave vector in the incident acoustic wave.

A.5. Excitation of short waves due to the acoustic wave dissipation

In Sec. A.2 - A.4, we have considered possible physical mechanisms of specular radar reflection caused by infrasound, when the acoustic wave dissipation per wavelength is weak. A different mechanism becomes efficient in the opposite regime, when significant absorption of infrasound occurs either due to wave breaking or dissipation of linear acoustic waves. When infrasound is absorbed, most of its mechanical energy is transformed into heat.

Dissipation of infrasound creates a spatially and temporally modulated heat source, which generates thermal waves. Transfer of the momentum of dissipating or breaking infrasound wave to the fluid (air) results in the spatially and temporally modulated source of external force, which contributes to the mean motion (wind) and can also generate viscous waves. The infrasound momentum transfer is arguably a less efficient contributor to the radar specular scattering than infrasound energy conversion into heat, and we will further discuss only the latter.

Let the acoustic wave have the harmonic dependence $\exp(ikx - i\omega t)$ on horizontal coordinates and time (in the same complex notation we have used above). Assuming that the infrasound dissipation rate is proportional to the square of (real) acoustic pressure, the resulting heat source has the double wave frequency 2ω and double horizontal wavenumber $2k$. In the absence of wind, it moves horizontally with the same speed ω/k as the acoustic wave. To illustrate the thermal waves generated by the moving source of heat, consider an idealized problem. Let an external heat source generate a temperature perturbation with the amplitude δT in a thin horizontal layer around $z = z_1$ in a homogeneous ideal gas with temperature T_0. In complex notations, the temperature at $z = z_1$ is

$$T = T_0 + \delta T \exp(2ikx - 2i\omega t). \tag{A26}$$

In the surrounding gas, the temperature equilibrates to the background value away from the source plane through thermal waves, leading to the following temperature distribution:

$$T(x,z,t) = T_0 + \delta T \times \exp\left(2i(kx - \omega t) + (i-1)\sqrt{\frac{\omega\rho_0 \mathrm{Pr}}{\eta}}|z - z_1|\right). \tag{A27}$$

Eq. (A27) follows from Eq. (A16) and the boundary conditions of temperature continuity at the boundaries of the thin heated layer. The vertical spatial scale of the temperature perturbations is smaller by the factor $2^{1/2}$ than in the thermal waves generated at reflection of the infrasound wave of frequency ω.

Since pressure is essentially constant in the thermal waves, the temperature variations in Eq. (A27) due to the modulated heating are accompanied by the mass density perturbations $\rho_1(x,z,t) = \left[1 - T_0^{-1} T(x,z,t)\right]\rho_0$ with the amplitude $\rho_0|\delta T|/T_0$. If δT is comparable to the amplitude of the temperature variations in the original acoustic wave, the mass density perturbations and the resulting electron density perturbations in Eq. (A2) are much stronger than due to the thermal waves, which are generated either at the infrasound wave propagation through a gradient layer or infrasound reflection from a sharp interface. It should be emphasized that, in contrast to the mechanisms considered

in Sec. A.2 and A.4, the specular radar reflections due to infrasound dissipation require strong gradients of neither the neutral atmosphere temperature nor the electron density. This is significant in view of the observation by Strelnikov et al. (2021) in the PMWE rocket campaign, that "detailed investigation of all the density and temperature profiles did not yield any sharp gradient in the regions of PMWE occurrence," which is needed to support generation of the viscous and thermal waves at reflection of either infrasound or gravity waves.

The turbulence generated by breaking of acoustic or gravity waves apparently lacks the coherence needed to explain the high-aspect ratio, fast propagating PMWE. However, acoustic energy dissipation at wave breaking would provide the heat sources with the necessary phase coherence and would potentially explain the coincidence of the regions of PMWE generation with the regions of high turbulence, as reported in Strelnikov et al. (2021) for other PMWE. If wave breaking depends on the sign of the acoustic pressure and density variations and occurs either at the throughs (acoustic pressure and density minima) or at the peaks (acoustic pressure and density maxima) of infrasonic waves, the above Eq. (A26) and Eq. (A27) would hold, but with k and ω replaced by $k/2$ and $\omega/2$, respectively.

The oscillatory velocity amplitude, the ratio of the acoustic wave amplitude to the ambient pressure as well as the ratio of the density perturbations in the linear acoustic wave to the ambient density all increase exponentially with the altitude due to the exponential decrease in the ambient density. For acoustic waves propagating to MLT from ground-level sources the likelihood of wave breaking is expected to be increased in the vicinity of the turning point of the acoustic rays, which are the highest-altitude part of the ray trajectory. The likelihood of the wave breaking is further increased by the acoustic field focusing that occurs in the vicinity of caustics and turning points (Brekhovskikh and Godin, 1999). All these factors, which lead to the increase in the wave amplitude, also contribute to enhanced dissipation of non-breaking, linear acoustic waves in the vicinity of the turning points. The acoustic wave dissipation and the heat deposition, which leads to thermal wave generation, is additionally enhanced in the vicinity of the turning points by exponential increase of the kinematic viscosity η/ρ_0 with altitude and the resulting exponential increase of the acoustic energy loss per unit path length (Sutherland and Bass, 2004; Godin, 2014). Thus, even without wave breaking, significant generation of the thermal waves, Eq. (A27), is expected in the vicinity of the turning points of infrasound rays. These thermal waves can further contribute to the coherent radar scattering as discussed in Sec. A.3.

So far, we assumed in Sec. A.2 - A.5 that there is no wind. To a good approximation, the effect of uniform wind or gradually varying with the altitude wind velocity $\boldsymbol{u}$ can be taken into account by replacing the acoustic frequency ω with the intrinsic frequency $\omega_d = \omega - \boldsymbol{k}\cdot\boldsymbol{u}$ (Godin, 2014). Rapid variations of the wind velocity require an additional analysis. Based on the close analogy between the theory of acoustic waves in motionless and moving horizontally stratified fluids (Brekhovskikh and Godin, 1998), it is expected that, in addition to replacing ω with ω_d, the effects of the strong gradients in the wind velocity can be approximately described by replacing $\rho_0^{-1}\partial\rho_0/\partial z$ with $\rho_0^{-1}\partial\rho_0/\partial z - 2\omega_d^{-1}\boldsymbol{k}\cdot\partial\boldsymbol{u}/\partial z$ in the equations in Sections A.2 - A.5.

References

Baumann, C., Rapp, M., Kero, A., Enell, C.F., 2013. Meteor smoke influences on the D-region charge balance - review of recent in situ measurements and one-dimensional model results. Ann. Geophys. 31, 2049–2062. https://doi.org/10.5194/angeo-31-2049-2013.

Baumgarten, G., Fiedler, J., Lübken, F.J., von Cossart, G., 2008. Particle properties and water content of noctilucent clouds and their interannual variation. Journal of Geophysical Research: Atmosphere 113. https://doi.org/10.1029/2007JD008884.

Belova, E., Kero, J., Näsholm, S. P., Vorobeva, E., Godin, O. A., Barabash, V., Kajtar, R., and Le Pichon, A. (2020). Polar mesosphere winter echoes and their relation to infrasound. Paper presented at EGU General Assembly 2020, online, Vienna, Austria, May 2020. doi: 10.5194/egusphere-egu2020-5055.

Belova, E., Voelger, P., Kirkwood, S., Hagelin, S., Lindskog, M., Körnich, H., Chatterjee, S., Satheesan, K., 2021. Validation of wind measurements of two mesosphere–stratosphere–troposphere radars in northern Sweden and in Antarctica. Journal of Atmospheric Measurement Techniques 14, 2813–2825. https://doi.org/10.5194/amt-14-2813-2021.

Benioff, H., Gutenberg, B., 1939. Waves and currents recorded by electromagnetic barographs. Bull. Am. Meteorol. Soc. 20 (10), 421–428. https://doi.org/10.1175/1520-0477-20.10.421.

Blixt, E.M., Näsholm, S.P., Gibbons, S.J., Evers, L.G., Charlton-Perez, A. J., Orsolini, Y.J., Kværna, T., 2019. Estimating tropospheric and stratospheric winds using infrasound from explosions. J. Acoust. Soc. Am. 146 (2), 973–982. https://doi.org/10.1121/1.5120183.

Bowman, D.C., Albert, S.A., 2018. Acoustic event location and background noise characterization on a free flying infrasound sensor network in the stratosphere. Geophys. J. Int. 213 (3), 1524–1535. https://doi.org/10.1093/gji/ggy069.

Brekhovskikh, L. M., and Godin, O. A. (1998). Acoustics of layered media I: Plane and quasi-plane waves (pp. 6–9, 144–149, 205–226). 2nd ed. Springer, Berlin, New York.

Brekhovskikh, L. M., and Godin, O. A. (1999). Acoustics of layered media. II: Point sources and bounded beams (pp. 209–241, 363–369). 2nd extended ed., Springer, Berlin, New York. doi: 10.1007/978-3-662-03889-5.

Brekhovskikh, L.M., Goncharov, V.V., Kurtepov, V.M., Naugolny, K.A., 1973. Radiation of infrasound into atmosphere by surface-waves in ocean. Izvestiya Akademii Nauk SSSR Fizika Atmosfery i Okeana 9 (9), 899–907.

Briggs, B.H., 1984. The analysis of spaced sensor records by correlation technique. In: Vincent, R.A. (Ed.), Middle Atmosphere Program, Handbook for MAP, 13: Ground-based Techniques. NASA, Washington, USA, pp. 166–186.

Briggs, B.H., Phillips, G.J., Shinn, D.H., 1950. The analysis of observations on spaced receivers of the fading of radio signals. Proceeding of the Physical Society 63B, 106–121.

Chilson, P.B., Kirkwood, S., Nilsson, A., 1999. The Esrange MST radar: A brief introduction and procedure for range validation using balloons. Radio Sci. 34, 427–436. https://doi.org/10.1029/1998RS900023.

Christie, D., Campus, P., 2010. In: The IMS Infrasound Network: Design and Establishment of Infrasound Stations. Springer, pp. 29–75. https://doi.org/10.1007/978-1-4020-9508-5_2.

Dahlman, O., Mykkeltveit, S., Haak, H., 2009. Nuclear test ban: converting political visions to reality. Springer Science and Business Media. https://doi.org/10.1007/978-1-4020-6885-0.

De Carlo, M., Ardhuin, F., Le Pichon, A., 2020. Atmospheric infrasound generation by ocean waves in finite depth: unified theory and application to radiation patterns. Geophys. J. Int. 221 (1), 569–585. https://doi.org/10.1093/gji/ggaa015.

De Carlo, M., Hupe, P., Le Pichon, A., Ceranna, L., Ardhuin, F., 2021. Global microbarom patterns: A first confirmation of the theory for source and propagation. Geophys. Res. Lett. 48 (3). https://doi.org/10.1029/2020GL090163 e2020GL090163.

Drob, D.P., Picone, J.M., Garcés, M., 2003. Global morphology of infrasound propagation. J. Geophys. Res. 108. https://doi.org/10.1029/2002JD003307.

Ecklund, W.L., Balsley, B.B., 1981. Long-term observations of the Arctic mesosphere with the MST radar at Poker Flat. Alaska, Journal of Geophysical Research 86. https://doi.org/10.1029/JA086iA09p07775.

ECMWF (2018), ERA5 model level, https://cds.climate.copernicus.eu/ Last accessed 22 March 2022.

Gage, K.S., Balsley, B.B., 1980. On the scattering and reflection mechanisms contributing to clear air radar echoes from the troposphere, stratosphere, and mesosphere. Radio Sci. 15 (2), 243–257. https://doi.org/10.1029/RS015i002p00243.

Gibbons, S., Kværna, T., Näsholm, P., 2019. In: Characterization of the Infrasonic Wavefield From Repeating Seismo-acoustic Events. Springer, pp. 387–407. https://doi.org/10.1007/978-3-319-75140-5_10.

Godin, O.A., 2002. An effective quiescent medium for sound propagating through an inhomogeneous, moving fluid. J. Acoust. Soc. Am. 112 (4), 1269–1275. https://doi.org/10.1121/1.1504853.

Godin, O.A., 2014. Dissipation of acoustic-gravity waves: An asymptotic approach, Journal of the Acoustic Society of. America 136 (6), EL411–EL417. https://doi.org/10.1121/1.4902426.

Godin, O.A., 2021. Shear waves and sound attenuation in underwater waveguides. Journal of the Acoustic Society of America 149 (5), 3586–3598. https://doi.org/10.1121/10.0004999.

Green, D. N., and A. Nippress, A. (2019). Infrasound signal duration: The effects of propagation distance and waveguide structure. Geophysical Journal International, 216(3), 1974–1988, ISSN 0956-540X. doi: 10.1093/gji/ggy530.

Hedlin, M., Walker, K., Drob, D., de Groot-Hedlin, C., 2012. Infrasound: Connecting the solid earth, oceans, and atmosphere. Annu. Rev. Earth Planet. Sci. 40, 327–354. https://doi.org/10.1146/annurev-earth-042711-105508.

Hersbach, H., Bell, B., Berrisford, P., Hirahara, S., Horányi, A., Muñoz-Sabater, J., Nicolas, J., Peubey, C., Radu, R., Schepers, D., Simmons, A., Soci, C., Abdalla, S., Abellan, X., Balsamo, G., Bechtold, P., Biavati, G., Bidlot, J., Bonavita, M., De Chiara, G., Dahlgren, P., Dee, D., Diamantakis, M., Dragani, R., Flemming, J., Forbes, R., Fuentes, M., Geer, A., Haimberger, L., Healy, S., Hogan, R.J., Hólm, E., Janisková, M., Keeley, S., Laloyaux, P., Lopez, P., Lupu, C., Radnoti, G., de Rosnay, P., Rozum, I., Vamborg, F., Villaume, S., Thépaut, J.-N., 2020. The ERA5 global reanalysis. Q. J. Roy. Meteor. Soc. 146, 1999–2049. https://doi.org/10.1002/qj.3803.

Hervig, M.E., Gordley, L.L., Stevens, M.H., Russell, J.M., Bailey, S.M., Baumgarten, G., 2009. Interpretation of SOFIE PMC measurements: cloud identification and derivation of mass density, particle shape, and particle size. J. Atmos. Sol. Terr. Phys. 71 (3–4), 316–330. https://doi.org/10.1016/j.jastp.2008.07.009.

Hocking, W.K., 2003. Evidence for viscosity, thermal conduction and diffusion waves in the Earth's atmosphere. Rev. Sci. Instrum. 74 (1). https://doi.org/10.1063/1.1516246.

Hocking, W.K., Fukao, S., Yamamoto, M., Tsuda, T., Kato, S., 1991. Viscosity waves and thermal-conduction waves as a cause of specular reflectors in radar studies of the atmosphere. Radio Sci. 26 (5), 1281–1303. https://doi.org/10.1029/91RS01661.

Holdsworth, D.A., 1995. Signal analysis with applications to atmospheric radars. University of Adelaide, Adelaide, Australia, p. 371 pp., PhD thesis.

Hupe, P., Ceranna, L., Pilger, C., De Carlo, M., Le Pichon, A., Kaifer, B., Rapp, M., 2019. Assessing the middle atmosphere weather models using infrasound detections from microbaroms. Geophys. J. Int. 216, 1761–1767. https://doi.org/10.1093/gji/ggy520.

Kavanagh, A.J., Honary, F., Donovan, E.F., Ulich, T., Denton, M., 2012. H.: Key features of > 30keV electron precipitation during high speed solar wind streams: A superposed epoch analysis. J. Geophysical Research 117, A00L09. https://doi.org/10.1029/2011JA017320.

Kirkwood, S., 2007. Polar Mesosphere WINTER Echoes: a review of recent results. J. Adv. Space Res. 40 (6), 751–757. https://doi.org/10.1016/j.asr.2007.01.024.

Kirkwood, S., Barabash, V., Belova, E., Nilsson, H., Rao, N., Stebel, K., Osepian, A., Chilson, P.B., 2002. Polar mesosphere winter echoes during solar proton events. Advances in Polar Upper Atmosphere Research 16, 111–125.

Kirkwood, S., Chilson, P.B., Belova, E., Dalin, P., Häggström, I., Rietveld, M., Singer, W., 2006. Infrasound – the cause of strong polar mesosphere winter echoes?. Ann. Geophys. 24, 475–491.

Kirkwood, S., Osepian, A., Belova, E., Lee, Y.S., 2015a. High-speed solar wind streams and polar mesosphere winter echoes at Troll, Antarctica. Ann. Geophys. 33, 609–622. https://doi.org/10.5194/angeo-33-609-2015.

Kirkwood, S., Osepian, A., Belova, E., Urban, J., Pérot, K., Sinha, A.K., 2015b. Ionization and NO production in the polar mesosphere during high-speed solar wind streams: model validation and comparison with NO enhancements observed by Odin-SMR. Ann. Geophys. 33, 561–572. https://doi.org/10.5194/angeo-33-561-2015.

[dataset] Kiruna riometers https://www2.irf.se/Observatory/?link=Riometers.

Landès, M., Le Pichon, A., Shapiro, N.M., Hillers, G., Campillo, M., 2014. Explaining global patterns of microbarom observations with wave action models. Geophys. J. Int. 199 (3), 1328–1337.

Latteck, R., Singer, W., Rapp, M., Vandepeer, B., Renkwitz, T., Zecha, M., Stober, G., 2012. MAARSY: the new MST radar on Andøya-System description and first results. Radio Sci. 47, 1006. https://doi.org/10.1029/2011RS004775.

Latteck, R., Strelnikova, I., 2015. Extended observations of polar mesosphere winter echoes over Andøya (69°N) using MAARSY. Journal Geophysical Research 120, 8216–8226. https://doi.org/10.1002/2015JD023291.

Latteck, R., Renkwitz, T., Chau, J.L., 2021. Two decades of long-term observations of polar mesospheric echoes at 69°N. J. Atmos. Sol. Terr. Phys. 216. https://doi.org/10.1016/j.jastp.2021.105576 105576.

Le Du, T., Simoneau, P., Keckhut, P., Hauchecorne, A., Le Pichon, A., 2020. Investigation of infrasound signatures from microbaroms using OH airglow and ground-based microbarometers. Adv. Space Res. 65 (3), 902–908. https://doi.org/10.1016/j.asr.2019.11.026.

Le Pichon, A., Blanc, E., Hauchecorne, A. (Eds.), 2010. Infrasound Monitoring for Atmospheric Studies. Springer Science & Business Media B.V, p. 735. https://doi.org/10.1007/978-1-4020-9508-5_7.

Longuet-Higgins, M.S., 1984. Statistical properties of wave groups in a random sea state. Philosophical Transactions of the Royal Society of London. Series A, Mathematical and Physical Sciences 312 (1521), 219–250.

Lonzaga, J.B., 2015. A theoretical relation between the celerity and trace velocity of infrasonic phases. J. Acoust. Soc. Am. 138 (3), EL242–EL247. https://doi.org/10.1121/1.4929628.

Lübken, F.J., 1999. Thermal structure of the arctic summer mesosphere. J. Geophys. Res. Atmos. 104 (D8), 9135–9149. https://doi.org/10.1029/1999JD900076.

Marty, J., 2019. The IMS infrasound network: current status and technological developments. In: Infrasound Monitoring for Atmospheric Studies. Springer, pp. 3–62.

Meredith, N.P., Horne, R.B., Lam, M.M., Denton, M.H., Borovsky, J.E., Green, J.C., 2011. Energetic electron precipitation during high-speed solar wind stream driven storms. J. Geophys. Res. 116, A05223. https://doi.org/10.1029/2010JA016293.

Nishiyama, T., Sato, K., Nakamura, T., Tsutsumi, M., Sato, T., Tanaka, Y.M., Nishimura, K., Tomikawa, Y., Kohma, M., 2018. Simultaneous observations of polar mesosphere winter echoes and cosmic noise absorptions in a common volume by the PANSY radar (69.0°S, 39.6° E). Journal of Geophysical Research: Space. Physics 123 (6), 5019–5032. https://doi.org/10.1029/2017JA024717.

Pierce, A.D., 1989. Acoustics: an introduction to its physical principles and applications, 2nd ed. Acoustical Society of America, Woodbury, New York, pp. 519–531.

Rapp, M., Lübken, F.J., 2004. Polar mesosphere summer echoes (PMSE): Review of observations and current understanding. Atmos. Chem. Phys. 4, 2601–2633. https://doi.org/10.5194/acp-4-2601-2004.

Rapp, M., Strelnikova, I., Strelnikov, B., Latteck, R., Baumgarten, G., Li, Q., Megner, L., Gumbel, J., Friedrich, M., Hoppe, U., Robertson, S., 2009. First in situ measurement of the vertical distribution of ice volume in a mesospheric ice cloud during the ECOMA/MASS rocket-campaign. Ann. Geophys. 27, 755–766 https://angeo.copernicus.org/articles/27/755/2009/angeo-27-755-2009.pdf.

Rind, D., Donn, W.L., Dede, E., 1973. Upper air wind speeds calculated from observations of natural infrasound. J. Atmos. Sci. 30 (8), 1726–1729. https://doi.org/10.1175/1520-0469.

Robertson, S., Dickson, S., Horányi, M., Sternovsky, Z., Friedrich, M., Janches, D., Megner, L., Williams, B., 2014. Detection of meteoric smoke particles in the mesosphere by a rocket-borne mass spectrometer. J. Atmos. Sol. Terr. Phys. 118, 161–179. https://doi.org/10.1016/j.jastp.2013.07.007.

Röttger, J., La Hoz, C., Kelley, M.C., Hoppe, U.P., Hall, C., 1988. The structure and dynamics of polar mesosphere summer echoes observed with the EISCAT 224 MHz radar. Geophys. Res. Lett. 15 (12), 1353–1356. https://doi.org/10.1029/GL015i012p01353.

Savel'ev, A. Ya., 1973. Konstantinov's effect in certain acoustical problems, Soviet Physics Acoustics, 19(2). UDK 534 (24), 231–239.

Smirnova, M., Belova, E., Kirkwood, S., 2012. Aspect sensitivity of polar mesosphere summer echoes based on ESRAD MST radar measurements in Kiruna, Sweden in 1997–2010. Annales Geophyicae. 30, 457–465. https://doi.org/10.5194/angeo-30-457-2012.

Space Weather Prediction Center, National Oceanic and Atmospheric Administration, https://www.swpc.noaa.gov/products/.

Staszak, T., Strelnikov, B., Latteck, R., Renkwitz, T., Friedrich, M., Baumgarten, G., Lübken, F.-J., 2021. Turbulence generated small-scale structures as PMWE formation mechanism: Results from a rocket campaign. J. Atmos. Sol. Terr. Phys. 217. https://doi.org/10.1016/j.jastp.2021.105559 105559.

Strelnikov, B., Staszak, T., Latteck, R., Renkwitz, T., Strelnikova, I., Lübken, F.-J., Baumgarten, G., Fiedler, J., Chau, J.L., Stude, J., Rapp, M., Friedrich, M., Gumbel, J., Hedin, J., Belova, E., Hörschgen-Eggers, M., Giono, G., Hörner, I., Löhle, S., Eberhart, M., Fasoulas, S., 2021. Sounding rocket project "PMWE" for investigation of polar mesosphere winter echoes. J. Atmos. Sol. Terr. Phys. 218. https://doi.org/10.1016/j.jastp.2021.105596.

Sutherland, L.C., Bass, H.E., 2004. Atmospheric absorption in the atmosphere up to 160 km. J. Acoust. Soc. Am. 115, 1012–1032. https://doi.org/10.1121/1.1631937.

Swarnalingam, N., Hocking, W.K., Drummond, J.R., 2011. Long-term aspect-sensitivity measurements of polar mesosphere summer echoes (PMSE) at Resolute Bay using a 51.5MHz VHF radar. J. Atmos. Sol. Terr. Phys. 73, 957–964. https://doi.org/10.1016/j.jastp.2010.09.032.

Tanaka, Y.M., Nishiyama, T., Kadokura, A., Ozaki, M., Miyoshi, Y., Shiokawa, K., et al., 2019. Direct comparison between magnetospheric plasma waves and polar mesosphere winter echoes in both hemispheres. J. Geophys. Res. Space Phys. 124, 9626–9639. https://doi.org/10.1029/2019JA026891.

The WAVEWATCH III:® Development Group (2016). User manual and system documentation of WAVEWATCH III ® version 5.16. Technical Note 329, NOAA/NWS/NCEP/MMAB, 326 pp, College Park, U.S.

Vergoz, J., Le Pichon, A., Millet, C., 2019. The Antares explosion observed by the USArray: an unprecedented collection of infrasound phases recorded from the same event. In: Infrasound Monitoring for Atmospheric Studies. Springer, pp. 349–386. https://doi.org/10.1007/978-3-319-75140-5_9.

Vorobeva, E., De Carlo, M., Le Pichon, A., Espy, P.J., Näsholm, S.P., 2021. Benchmarking microbarom radiation and propagation model against infrasound recordings: a vespagram-based approach. Ann. Geophys. 39 (3), 515–531. https://doi.org/10.5194/angeo-39-515-2021.

Waxler, R., Gilbert, K. E., Talmadge, C., and Hetzer, C. 2007. The effects of the finite depth of the ocean on microbarom signals. Paper presented at 8th International Conference on Theoretical and Computational Acoustics (ICTCA), Crete, Greece.